JOURNAL OF GEOPHYSICAL RESEARCH, VOL. 102, NO. D14, PAGES 16,989–17,013, JULY 27, 1997

Satellite retrieval of aerosol properties over the ocean using polarization as well as intensity of reflected sunlight

Michael I. Mishchenko

NASA Goddard Institute for Space Studies, New York, and Institute of Terrestrial and Planetary Atmospheres/State University of New York at Stony Brook

Larry D. Travis

NASA Goddard Institute for Space Studies, New York

Abstract. Most current and proposed satellite remote sensing of tropospheric aerosols relies upon radiance measurements that are interpreted using algorithms that determine best fits to precalculated scattered sunlight for one or more "standard" aerosol models. However, the number of different types of aerosol and the substantial space and time variations typically encountered can pose a severe uniqueness problem even for the multiple constraints provided by multispectral radiances of a scene at a number of observation zenith angles. Experience with polarimetry remote sensing on planetary missions has demonstrated that the measurement of polarization as well as the radiance can resolve such uniqueness problems. We use numerically accurate solutions of the vector radiative transfer equation for a realistic atmosphere-ocean model to theoretically simulate several types of satellite aerosol retrievals over the ocean utilizing radiance measurements alone, polarization measurements alone, and radiance and polarization measurements combined. We have restricted all simulations to a single near-infrared wavelength of 0.865 μm and assumed that aerosols are spherical, monomodal, and nonabsorbing. These simplifications permit a study of practical scope that tests the retrieval algorithms under exactly the same conditions, thus clearly demonstrating their relative capabilities. In agreement with previous analyses, we have found that radiance-only algorithms using multiple-viewing-angle observations perform far better than those based on single-viewing-angle measurements. However, even multiple-viewing-angle radiance measurements taken at a single wavelength are not always sufficient to determine the aerosol optical thickness, effective radius, and refractive index with high enough accuracy. In contrast, high-accuracy, single-wavelength, multiple-viewing-angle polarimetry alone is capable of uniquely retrieving all three aerosol characteristics with extremely high accuracy (±0.015 in aerosol optical thickness, ±0.03 μm in effective radius, and ±0.01 in refractive index). Furthermore, the accuracy of the optical thickness retrieval can be slightly improved by simultaneously using radiance measurements. Our analysis demonstrates that algorithms utilizing high-accuracy polarization as well as radiance measurements are much less dependent on the availability and use of a priori information and can be expected to provide a physically based retrieval of aerosol characteristics (optical thickness, refractive index, and size) with accuracy needed for long-term monitoring of global climate forcings and feedbacks.

1. Introduction

Tropospheric aerosols can affect the Earth's climate directly (by scattering and absorbing solar and terrestrial radiation) and indirectly (by altering cloud properties) and are considered the source of greatest present uncertainty in climate forcing [*Hansen and Lacis*, 1990; *Charlson et al.*, 1992; *Penner et al.*, 1994]. Accurate evaluation of the direct and indirect effects of tropospheric aerosols on climate requires precise global information on aerosol properties such as optical thickness, size distribution, refractive index, phase, and chemical composition [*Lacis and Mishchenko*, 1995; *Toon*, 1995]. Such global information can only be acquired using satellite passive and/or active remote sensing [*Karl*, 1995]. Most of the current [*Rao et al.*, 1989] and planned [*Diner et al.*, 1991; *Hooker et al.*, 1992; *King et al.*, 1992] satellite remote sensing relies upon radiance measurements that are interpreted using algorithms that determine best fits to precalculated scattered sunlight for one or more "standard" aerosol models [e.g., *Kaufman*, 1995]. However, the number of different types of aerosol and the substantial space and

Paper number 96JD02425.
0148-0227/97/96JD-02425$09.00

time variations typically encountered can pose a severe uniqueness problem even for the multiple constraints provided by multispectral radiances of a scene at one or even a number of observation zenith angles. This can make problematic the determination of the aerosol properties with accuracy necessary for long-term monitoring of global climate forcings and radiative feedbacks [*DelGenio*, 1993; *Hansen et al.*, 1995].

Previous experience with ground-based and spacecraft polarimetric remote sensing of planetary atmospheres [e.g., *Hansen and Hovenier*, 1974; *Kawabata et al.*, 1980; *Tomasko and Doose*, 1984; *Santer et al.*, 1986; *West and Smith*, 1991; *Sato et al.*, 1996] has demonstrated that the measurement of polarization as well as the radiance can successfully resolve such uniqueness problems. The advantage of polarimetry is both the very high measurement accuracy possible because linear polarization is a ratio of two orthogonal intensity components and the fact that polarization is very sensitive to particle microphysics [*Hansen and Travis*, 1974]. The Earth Observing System (EOS) Earth observing scanning polarimeter (EOSP) is based on design heritage developed for planetary missions and is expected to provide accurate global retrievals of tropospheric aerosol characteristics from high-precision multispectral and multiple-viewing-angle measurements of radiance and polarization [*Travis*, 1992, 1993]. EOSP is designed to scan a 12-mrad instantaneous field of view (10 km at nadir) from limb to limb through nadir, providing approximately 180 measurements of radiance and polarization over each scan in each of 12 narrow spectral bands covering the spectral range from 0.41 to 2.25 μm. The instrument can be mounted on the EOS spacecraft so that the scan is either along the spacecraft ground track or in the perpendicular, cross-track direction. We expect to adopt the along-track scanning orientation in order to obtain the most sensitive aerosol retrieval at the expense of the more rapid global coverage provided by the cross-track strategy. Along-track scanning yields views of a given location from a continuous range of zenith and scattering angles as the spacecraft passes overhead. Another important characteristic of EOSP is that it is self-calibrating to high precision. Using an inflight calibrator system employing tungsten-filament lamps and Rochon polarizers oriented in several directions, EOSP calibrates polarization to 0.2% absolute accuracy. These internal lamps, with a demonstrated stability of better than 2% per decade on a predecessor instrument, should provide a decadal precision for radiance of better than 0.002 for a reflectivity of 0.1. Currently, the instrument is scheduled to fly on the EOS AM-2 Platform in 2004. Another polarimeter, the polarization and directionality of the Earth's reflectances (POLDER) instrument developed in France [*Deschamps et al.*, 1994], is scheduled to fly aboard the Japanese Advanced Earth Observing Satellite (ADEOS) in 1996.

The purpose of this paper is to describe the theoretical basis of EOSP aerosol retrievals over the ocean and to illustrate in detail why polarization is so sensitive to aerosol properties and, in conjunction with intensity, provides a much more powerful remote sensing tool than radiance alone. In the following section, we introduce the basic polarimetric definitions and describe the atmosphere-ocean model and the computational technique used in our theoretical simulations. In section 3 we briefly discuss the dependence of aerosol single-scattering properties on particle size and refractive index. Following *Hansen and Travis* [1974], we demonstrate that single-scattering polarization is a much more sensitive function of particle microstructure than the scattering phase function, thus explaining the potentially much greater effectiveness of remote sensing by means of polarimerty. Since high-precision polarization measurements of the Earth's atmosphere are currently unavailable, in section 4 we employ numerically accurate solutions of the vector radiative transfer equation to theoretically simulate EOSP aerosol retrievals for a cloud-free atmosphere above a rough ocean surface. These simulations are used to compare the sensitivity to aerosol properties of single- and multiple-viewing-angle measurements of radiance alone, polarization alone, and combined radiance and polarization. We demonstrate that high-accuracy polarimetry can resolve the uniqueness problem inherent in retrieval techniques based on radiance measurements only and is crucial for reliable retrievals of aerosol optical thickness and, especially, aerosol size and refractive index with accuracy required for long-term climate monitoring.

2. Polarimetric Definitions, Atmosphere-Ocean Model, and Computational Technique

We assume that the atmosphere-ocean system is plane-parallel, i.e., the optical properties of the atmosphere and the ocean depend on only the vertical coordinate. To describe the geometry of multiple light scattering, we use a right-handed Cartesian coordinate system with the z axis directed along the outward normal to the upper boundary of the atmosphere, as shown in Figure 1. The direction of light propagation is specified by the unit vector $\boldsymbol{n}$ or, equivalently, by the couple (u, φ), where $u = -\cos\vartheta$, ϑ is the zenith angle measured from the positive z axis, and φ is the azimuth angle measured from the positive x axis in the clockwise direction when looking upward. Note that $u < 0$ for upwelling radiation and $u > 0$ for downwelling radiation. Also, we define $\mu = |u|$. To describe the intensity and state

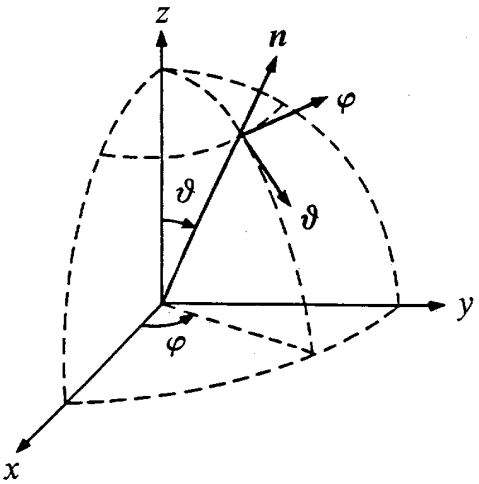

Figure 1. Schematic of the geometry of light scattering in the atmosphere-ocean system.

of polarization of a beam of light, we use the local right-handed orthonormal system formed by the unit vectors $\boldsymbol{n}$, $\boldsymbol{\vartheta}$, and $\boldsymbol{\varphi}$ given by

$$\boldsymbol{\varphi} = \frac{\boldsymbol{z}\times\boldsymbol{n}}{|\boldsymbol{z}\times\boldsymbol{n}|} \tag{1}$$

and

$$\boldsymbol{\vartheta} = \boldsymbol{\varphi}\times\boldsymbol{n}, \tag{2}$$

where $\boldsymbol{z}$ is a unit vector in the positive z direction. In other words, the unit vector $\boldsymbol{\vartheta}$ lies in the meridian plane of the beam (the plane through the beam and the local z axis), while the unit vector $\boldsymbol{\varphi}$ is perpendicular to this plane. Note that

$$\boldsymbol{n} = \boldsymbol{\vartheta}\times\boldsymbol{\varphi}. \tag{3}$$

Following *Hansen and Travis* [1974] and *Hovenier and van der Mee* [1983], we define, up to a multiplicative constant, the Stokes parameters I, Q, U, and V of a quasi-monochromatic beam of light as

$$I = \langle E_\vartheta E_\vartheta^* + E_\varphi E_\varphi^* \rangle, \tag{4}$$

$$Q = \langle E_\vartheta E_\vartheta^* - E_\varphi E_\varphi^* \rangle, \tag{5}$$

$$U = -\langle E_\vartheta E_\varphi^* + E_\varphi E_\vartheta^* \rangle, \tag{6}$$

$$V = i\langle E_\varphi E_\vartheta^* - E_\vartheta E_\varphi^* \rangle, \tag{7}$$

where E_ϑ and E_φ are the ϑ and φ components of the electric field, respectively, the asterisk denotes the complex-conjugate value, and angular brackets denote time averaging. The first Stokes parameter, I, is the common intensity, while the other three Stokes parameters specify the state of polarization of the beam of light.

The Stokes parameters of sunlight reflected by the atmosphere-ocean system are given by

$$I(-\mu,\varphi) = \mu_0 R_{11}(\mu,\mu_0,\varphi-\varphi_0)F_0, \tag{8}$$

$$Q(-\mu,\varphi) = \mu_0 R_{21}(\mu,\mu_0,\varphi-\varphi_0)F_0, \tag{9}$$

$$U(-\mu,\varphi) = \mu_0 R_{31}(\mu,\mu_0,\varphi-\varphi_0)F_0, \tag{10}$$

$$V(-\mu,\varphi) = \mu_0 R_{41}(\mu,\mu_0,\varphi-\varphi_0)F_0, \tag{11}$$

where (μ_0, φ_0) and $(-\mu, \varphi)$ specify the directions of light incidence and reflection, respectively; the incident sunlight is assumed to be unpolarized; πF_0 is the incident flux per unit area perpendicular to the incident beam; and $R_{ij}(\mu,\mu_0,\varphi-\varphi_0)$ are elements of the so-called reflection matrix of dimension (4×4) [*Hansen and Travis*, 1974]. Note that the reflection matrix relates the Stokes parameters of the incident and scattered beams specified with respect to their local meridian planes rather than with respect to the scattering plane (namely, the plane through the incident and reflected beams). Since we assume that the scattering medium comprises spherical or randomly oriented nonspherical particles, the reflection matrix depends on the difference between the azimuth angles of the incident and reflected beams rather than on each of the azimuth angles separately.

As was shown by *de Haan et al.* [1987], a convenient and efficient way of treating the azimuthal dependence of the reflection matrix is to expand it in a special Fourier series:

$$\begin{aligned}\boldsymbol{R}(\mu,\mu_0,\varphi-\varphi_0) = {} & \frac{1}{4}\sum_{m=0}^{M}\left(2-\delta_{m0}\right)\\ & \times\left\{\left[(\boldsymbol{E}+\boldsymbol{D})\boldsymbol{R}^m(\mu,\mu_0)(\boldsymbol{E}+\boldsymbol{D})\right.\right.\\ & \left.+(\boldsymbol{E}-\boldsymbol{D})\boldsymbol{R}^m(\mu,\mu_0)(\boldsymbol{E}-\boldsymbol{D})\right]\cos m(\varphi-\varphi_0)\\ & +\left[(\boldsymbol{E}-\boldsymbol{D})\boldsymbol{R}^m(\mu,\mu_0)(\boldsymbol{E}+\boldsymbol{D})\right.\\ & \left.\left.-(\boldsymbol{E}+\boldsymbol{D})\boldsymbol{R}^m(\mu,\mu_0)(\boldsymbol{E}-\boldsymbol{D})\right]\sin m(\varphi-\varphi_0)\right\},\end{aligned} \tag{12}$$

where

$$\boldsymbol{E} = \mathrm{diag}[1,1,1,1], \tag{13}$$

$$\boldsymbol{D} = \mathrm{diag}[1,1,-1,-1], \tag{14}$$

and the upper summation limit M depends on the desired accuracy of computations. We compute the Fourier components of the reflection matrix $\boldsymbol{R}^m$ for an aerosol-gas atmosphere above the ocean surface by solving numerically the invariant imbedding equation [*Hansen and Travis*, 1974]

$$\begin{aligned}\frac{d\boldsymbol{R}^m(\tau;\mu,\mu_0)}{d\tau} = {} & -\left[\frac{1}{\mu}+\frac{1}{\mu_0}\right]\boldsymbol{R}^m(\tau;\mu,\mu_0)\\ & +\frac{w}{4\mu\mu_0}\boldsymbol{Z}^m(-\mu,\mu_0)\\ & +\frac{w}{2\mu_0}\int_0^1 d\mu'\,\boldsymbol{R}^m(\tau;\mu,\mu')\boldsymbol{Z}^m(\mu',\mu_0)\\ & +\frac{w}{2\mu}\int_0^1 d\mu'\,\boldsymbol{Z}^m(-\mu,-\mu')\boldsymbol{R}^m(\tau;\mu',\mu_0)\\ & +w\int_0^1\int_0^1 d\mu'\,d\mu''\,\boldsymbol{R}^m(\tau;\mu,\mu')\\ & \times\boldsymbol{Z}^m(\mu',-\mu'')\boldsymbol{R}^m(\tau;\mu'',\mu_0),\end{aligned} \tag{15}$$

which describes the change of the reflection matrix when a new layer of incremental optical thickness $d\tau$ is added on top of the atmosphere with optical thickness τ. The scattering properties of the aerosol-gas mixture in the infinitesimally thin layer are described by the albedo for single scattering w and (4×4) matrices $\boldsymbol{Z}^m(u,u')$, which are Fourier components of the phase matrix $\boldsymbol{Z}(u,u',\varphi-\varphi')$. The phase matrix describes the angular distribution and the change of polarization state of light singly scattered by a small-volume element and relates the Stokes parameters of the incident and scattered beams specified with respect to their own meridian planes. Note that the invariant imbedding equation is especially suitable for computing the reflection matrix for vertically inhomogeneous atmospheres with arbitrary vertical

dependence of scattering properties. Although our application here is for the homogeneous case, the invariant imbedding approach still has an advantage over the standard adding/doubling method [*de Haan et al.*, 1987], since it generates the many optical thickness values (see section 4) in one run. Equation (15) is supplemented by the initial condition

$$\boldsymbol{R}^m(0;\mu,\mu_0) = \boldsymbol{R}_o^m(\mu,\mu_0), \tag{16}$$

where $\boldsymbol{R}_o^m$ are Fourier components of the reflection matrix of the ocean. Equation (16) assumes that the ocean reflection matrix is azimuthally symmetric and thus can also be expanded in a Fourier series analogous to the expansion of equation (12). All simulated retrievals described in section 4 below are for the single wavelength $\lambda = 0.865$ μm at which the contribution to the observed total radiance by photons that enter the ocean body and are then scattered upward is negligibly small [*Gordon and Wang*, 1994]. Therefore the matrices $\boldsymbol{R}_o^m(\mu,\mu_0)$ are just equal to the Fourier components of the reflection matrix of the rough ocean surface. We compute the ocean surface reflection matrix using the standard Kirchhoff approach under the stationary phase approximation [*Ulaby et al.*, 1982; *Tsang et al.*, 1985] assuming the isotropic Gaussian distribution of surface slopes

$$p\left(\frac{\partial z}{\partial x},\frac{\partial z}{\partial y}\right) = \frac{1}{2\pi s^2}\exp\left(-\frac{\left(\frac{\partial z}{\partial x}\right)^2+\left(\frac{\partial z}{\partial y}\right)^2}{2s^2}\right), \tag{17}$$

in which the mean square surface slope s^2 is related to the near-surface wind speed W (in meters per second) by the empirical formula [*Cox and Munk*, 1954]

$$2s^2 = 0.003 + 0.00512\,W. \tag{18}$$

The Kirchhoff approach is applicable to surfaces with undulations whose average dimension is large compared to the wavelength of light and is essentially equivalent to the geometric optics approach used by *Ahmad and Fraser* [1982], *Nakajima and Tanaka* [1983], *Takashima* [1985], and *Deuzé et al.* [1989].

The Fourier components of the phase matrix are given by [*de Haan et al.*, 1987]

$$\boldsymbol{Z}^m(u,u') = (-1)^m \sum_{s=m}^{s_{max}} \boldsymbol{P}_m^s(u)\boldsymbol{S}^s\boldsymbol{P}_m^s(u'), \quad u,u' \in [-1,1]. \tag{19}$$

The matrices $\boldsymbol{P}_m^s(u)$ are defined as

$$\boldsymbol{P}_m^s(u) = \begin{bmatrix} P_{m0}^s(u) & 0 & 0 & 0 \\ 0 & P_{m+}^s(u) & P_{m-}^s(u) & 0 \\ 0 & P_{m-}^s(u) & P_{m+}^s(u) & 0 \\ 0 & 0 & 0 & P_{m0}^s(u) \end{bmatrix} \tag{20}$$

and

$$P_{m\pm}^s(u) = \frac{1}{2}\left[P_{m,-2}^s(u) \pm P_{m2}^s(u)\right], \tag{21}$$

where $P^s_{mn}(u)$ are generalized spherical functions [*Hovenier and van der Mee*, 1983]. The matrices $\boldsymbol{S}^s$ have the form

$$\boldsymbol{S}^s = \begin{bmatrix} a_1^s & b_1^s & 0 & 0 \\ b_1^s & a_2^s & 0 & 0 \\ 0 & 0 & a_3^s & b_2^s \\ 0 & 0 & -b_2^s & a_4^s \end{bmatrix}. \tag{22}$$

The elements of these matrices are the coefficients that appear in the following expansions:

$$a_1(\Theta) = \sum_{s=0}^{s_{max}} a_1^s\, P_{00}^s(\cos\Theta), \tag{23}$$

$$a_2(\Theta)+a_3(\Theta) = \sum_{s=2}^{s_{max}} \left(a_2^s+a_3^s\right) P_{22}^s(\cos\Theta), \tag{24}$$

$$a_2(\Theta)-a_3(\Theta) = \sum_{s=2}^{s_{max}} \left(a_2^s-a_3^s\right) P_{2,-2}^s(\cos\Theta), \tag{25}$$

$$a_4(\Theta) = \sum_{s=0}^{s_{max}} a_4^s\, P_{00}^s(\cos\Theta), \tag{26}$$

$$b_1(\Theta) = \sum_{s=2}^{s_{max}} b_1^s\, P_{02}^s(\cos\Theta), \tag{27}$$

$$b_2(\Theta) = \sum_{s=2}^{s_{max}} b_2^s\, P_{02}^s(\cos\Theta), \tag{28}$$

where Θ is the scattering angle (angle between the incident and scattered beams) and the functions $a_1(\Theta)$ to $b_2(\Theta)$ are the elements of the scattering matrix:

$$\boldsymbol{F}(\Theta) = \begin{bmatrix} a_1(\Theta) & b_1(\Theta) & 0 & 0 \\ b_1(\Theta) & a_2(\Theta) & 0 & 0 \\ 0 & 0 & a_3(\Theta) & b_2(\Theta) \\ 0 & 0 & -b_2(\Theta) & a_4(\Theta) \end{bmatrix}. \tag{29}$$

The (1,1) element of the scattering matrix, $a_1(\Theta)$, is called the scattering phase function and satisfies the normalization condition

$$\frac{1}{2}\int_0^\pi d\Theta \sin\Theta\, a_1(\Theta) = 1. \tag{30}$$

The scattering matrix relates the Stokes parameters of the incident and scattered beams specified with respect to the scattering plane, i.e., the plane through the two beams, whereas the phase matrix $\boldsymbol{Z}(u,u',\varphi-\varphi')$ is referenced to local meridian planes of the beams. The relationship between the

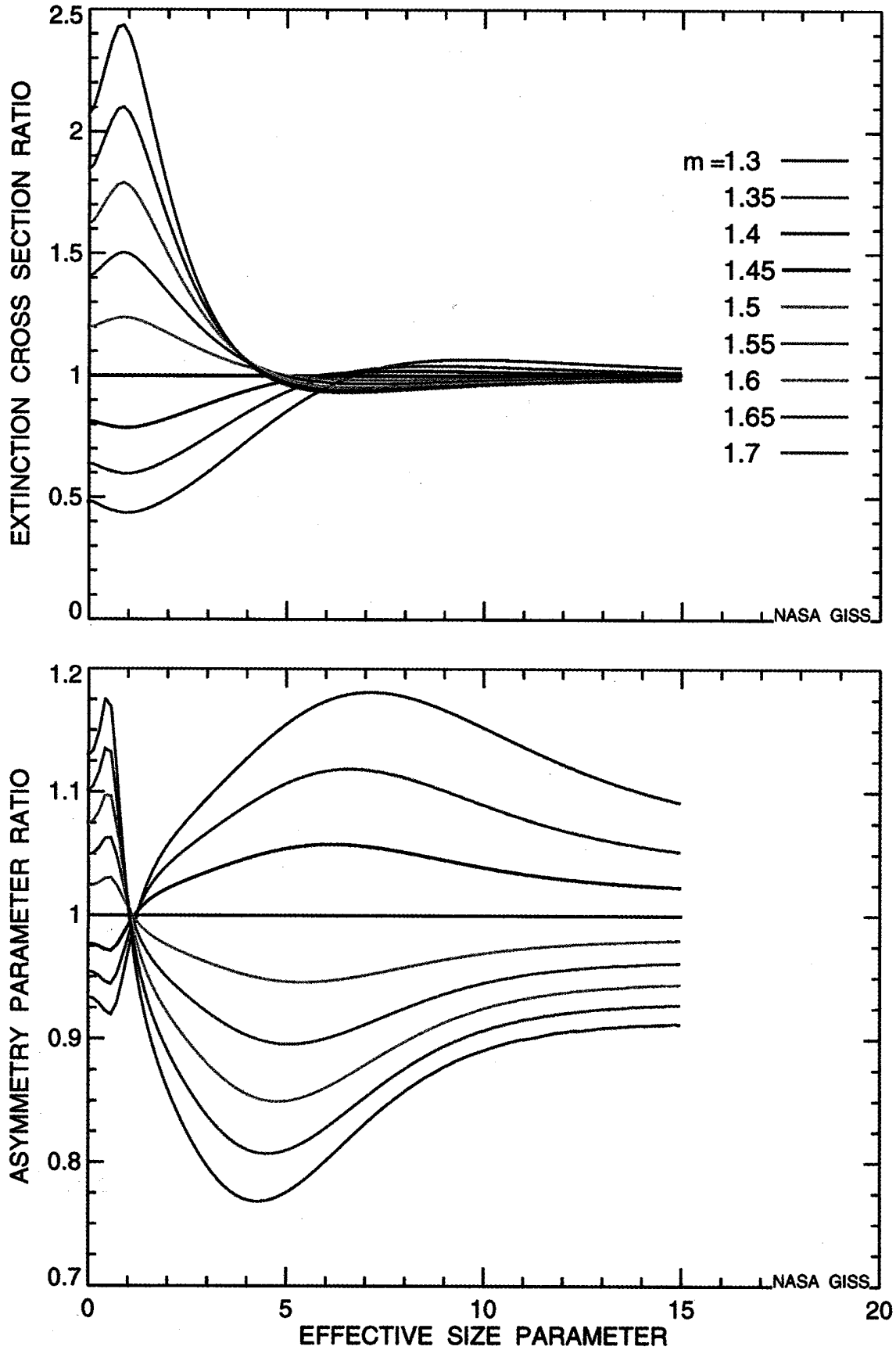

Plate 1. The upper panel shows the ratio $C_{ext}(x_{eff}; m)/C_{ext}(x_{eff}; 1.45)$ of the extinction cross sections for polydisperse spherical particles with refractive index m relative to that for particles with $m = 1.45$. These computations assume a gamma size distribution with the effective variance $v_{eff} = 0.2$. The lower panel is the same as the upper panel, except for the asymmetry parameter ratio $g(x_{eff}; m)/g(x_{eff}; 1.45)$.

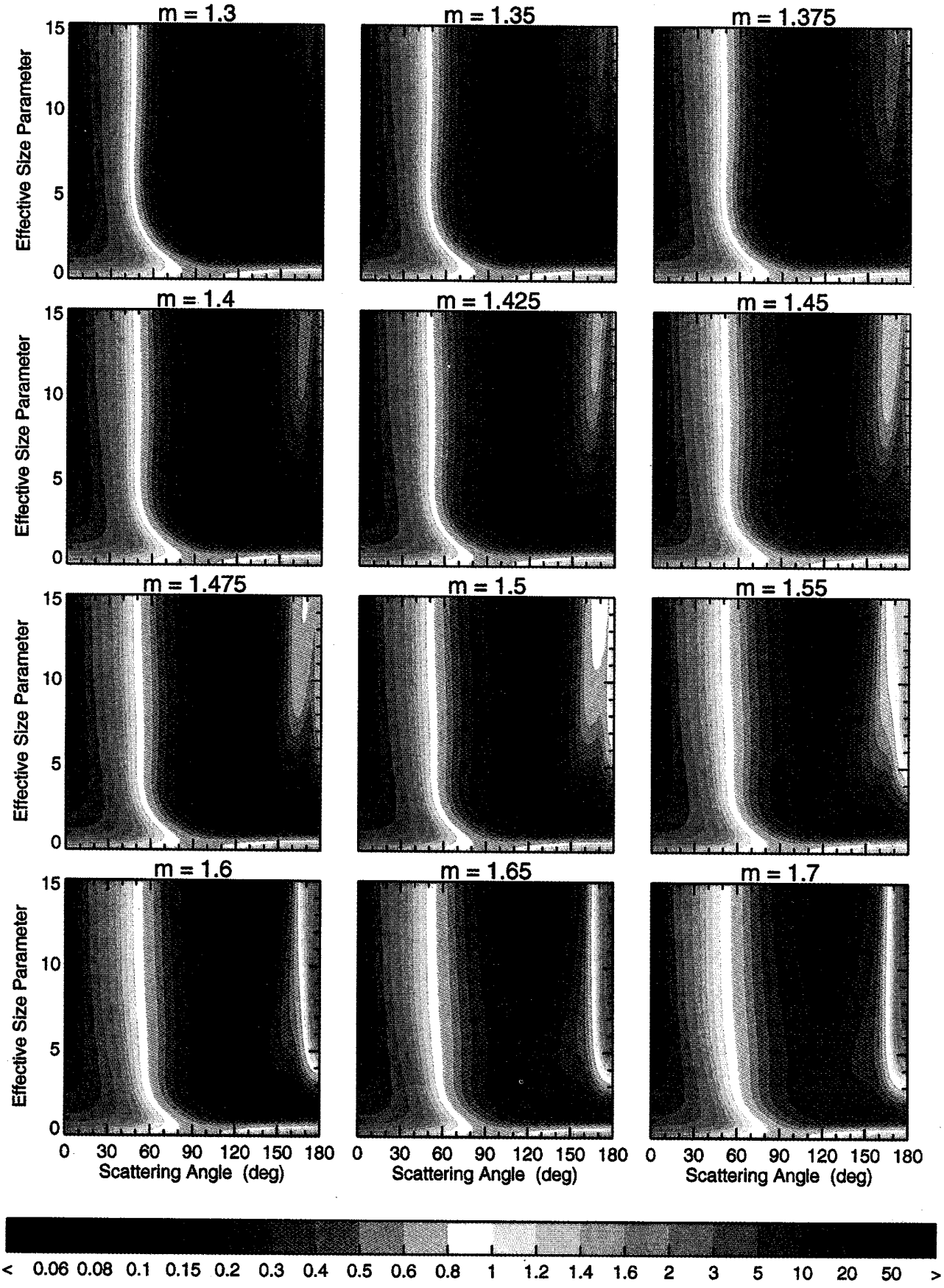

Plate 2. Color contour diagrams of the scattering phase function $a_1(\Theta)$ versus scattering angle and effective size parameter for a gamma distribution of spherical aerosols with effective variance $v_{eff} = 0.2$ and refractive index m varying from 1.3 to 1.7.

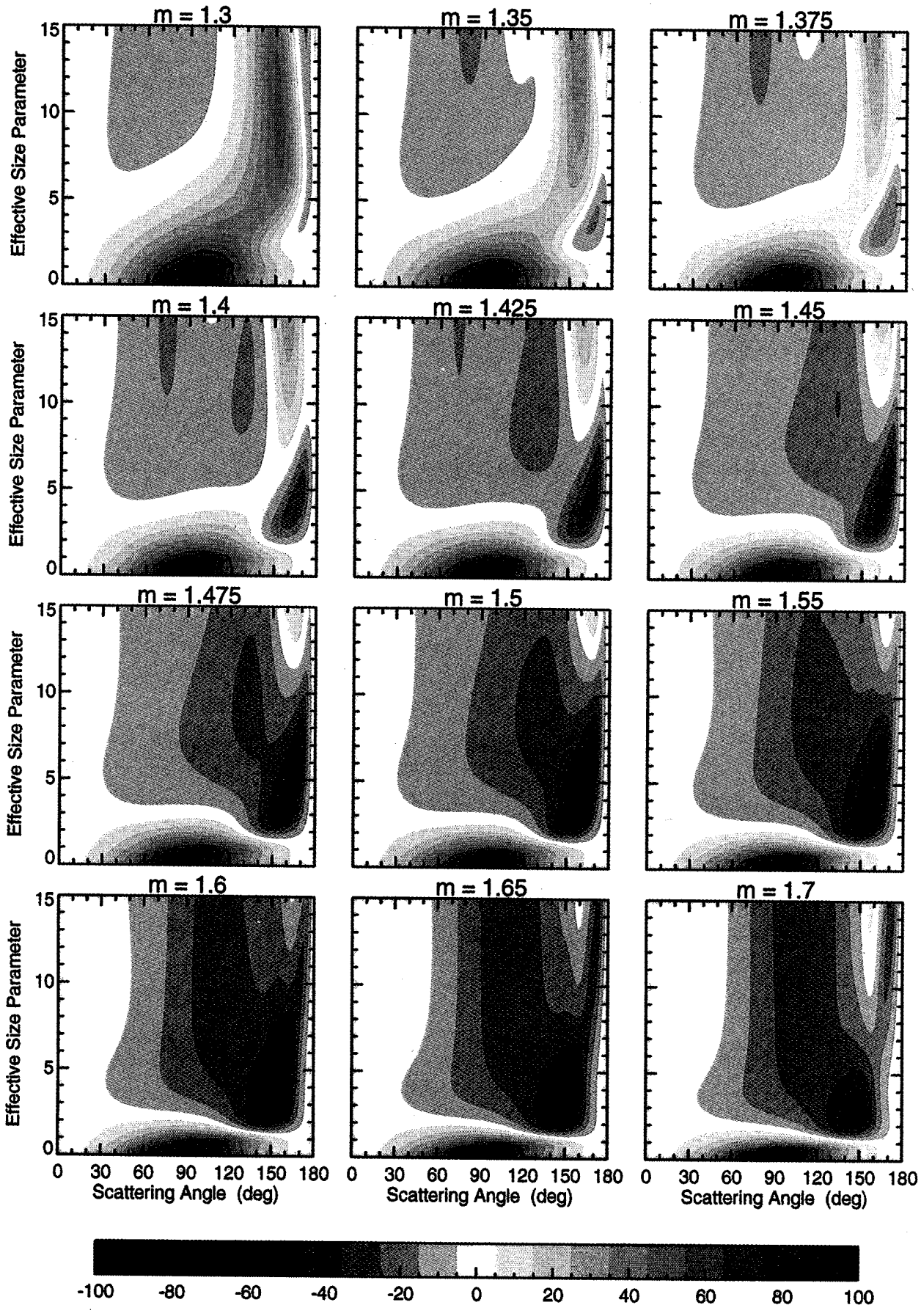

Plate 3. As in Plate 2, except for the degree of linear polarization $-b_1(\Theta)/a_1(\Theta)$ (%).

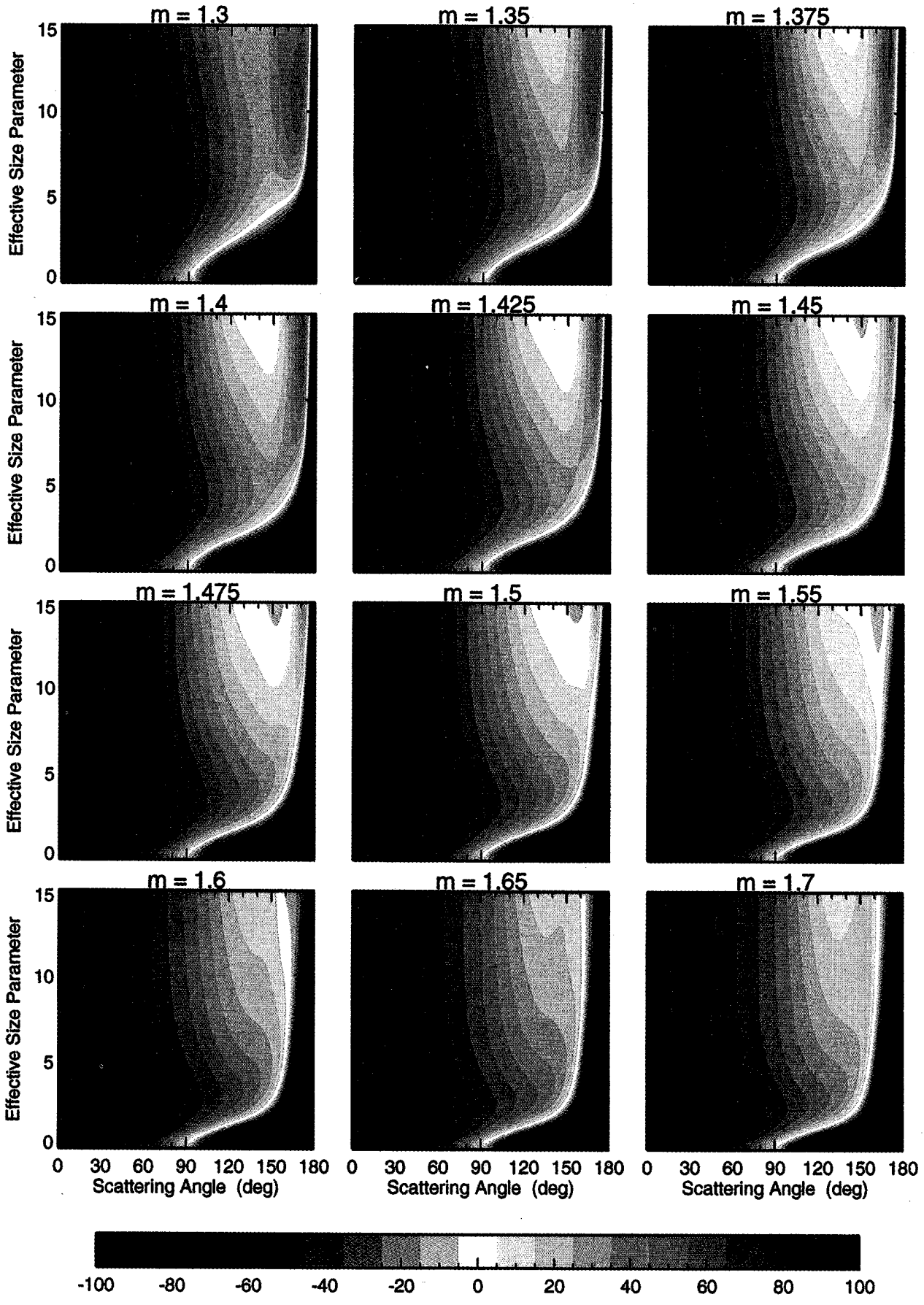

Plate 4. As in Plate 2, except for the ratio $a_3(\Theta)/a_1(\Theta)$ (%).

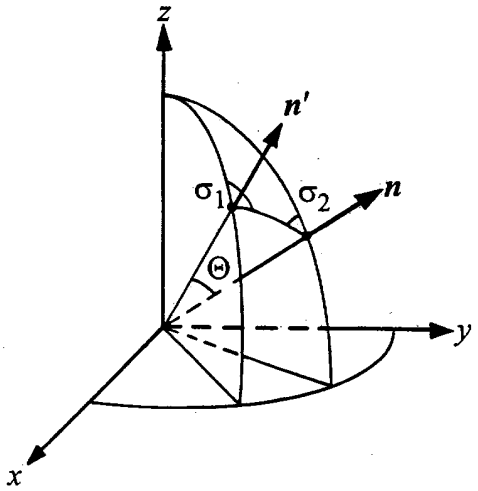

Figure 2. On the relationship between the scattering and phase matrices.

two matrices is given by

$$\boldsymbol{Z}(\boldsymbol{n},\boldsymbol{n}')\equiv\boldsymbol{Z}(u,u',\varphi-\varphi')=\boldsymbol{L}(\sigma_2)\,\boldsymbol{F}(\Theta)\,\boldsymbol{L}(\sigma_1), \quad (31)$$

where the (4×4) rotation matrix is defined as

$$\boldsymbol{L}(\sigma) = \begin{bmatrix} 1 & 0 & 0 & 0 \\ 0 & \cos 2\sigma & \sin 2\sigma & 0 \\ 0 & -\sin 2\sigma & \cos 2\sigma & 0 \\ 0 & 0 & 0 & 1 \end{bmatrix}, \quad (32)$$

and the angles σ_1 and σ_2 are shown in Figure 2. The block-diagonal form of the scattering matrix of equation (29) implies that the particles comprising a small-volume element are randomly oriented and have a plane of symmetry and/or are a mixture of particles and their mirror particles in equal numbers and in random orientation [*van de Hulst*, 1957]. Obviously, isotropic spheres satisfy either of these criteria. Note that equation (23) is the standard expansion of the phase function in Legendre polynomials [*van de Hulst*, 1980].

The computation of the reflection matrix for the ocean-atmosphere system consists of the following five major numerical steps.

1. Calculation of the Fourier components of the ocean surface reflection matrix for a given value of the mean square surface slope using the formulas of the appendix.

2. Calculation of the single-scattering albedo w and the expansion coefficients appearing in expansions (23)-(28) for a given gas-aerosol model. Fast numerical techniques for computing the expansion coefficients for polydisperse spherical particles based on Mie theory are discussed by *de Rooij and van der Stap* [1984], while an efficient computational method for polydisperse, randomly oriented, rotationally symmetric nonspherical particles has been developed by *Mishchenko* [1993] (see also *Mishchenko et al.* [1996]). The single-scattering albedo and the expansion coefficients for a gas-aerosol mixture are given by

$$w = \frac{k_{\mathrm{sca,g}}+k_{\mathrm{sca,a}}}{k_{\mathrm{ext,g}}+k_{\mathrm{ext,a}}}, \quad (33)$$

$$a_1^s = \frac{k_{\mathrm{sca,g}}}{k_{\mathrm{sca,g}}+k_{\mathrm{sca,a}}}a_{1,\mathrm{g}}^s + \frac{k_{\mathrm{sca,a}}}{k_{\mathrm{sca,g}}+k_{\mathrm{sca,a}}}a_{1,\mathrm{a}}^s, \quad (34)$$

and similarly for other expansion coefficients, where the indices g and a label quantities pertaining to the gas and aerosol components, respectively, and k_{ext} and k_{sca} are the extinction and scattering coefficients per unit volume. The expansion coefficients for the gas component are given in Table 1 adapted from *de Rooij* [1985], in which

$$c = \frac{2(1-\delta)}{2+\delta} \quad (35)$$

and

$$d = \frac{2(1-2\delta)}{2+\delta}, \quad (36)$$

where δ is the depolarization factor. For air at visible wavelengths, δ is close to 0.03.

3. Computation of the Fourier components of the phase matrix via equations (19)-(21). Efficient recurrence relations for computing the generalized spherical functions are given by *de Haan et al.* [1987].

4. Computation of the Fourier components of the reflection matrix of the atmosphere-ocean system by solving numerically the initial value problem given by equations (15) and (16). In our computations, we employ the fast invariant imbedding method developed by *Sato et al.* [1977] for the scalar case (i.e., when polarization of multiply scattered light is ignored) and extended to the vector case by *Mishchenko* [1990, 1991].

5. Calculation of the total reflection matrix for the atmosphere-ocean system via equation (12).

We use several numerical recipes to significantly enhance the efficiency and accuracy of the computer code.

1. The energy conservation is ensured by renormalizing the zeroth Fourier component of the phase matrix as suggested by *Hansen* [1971] (see also *Wiscombe* [1976]).

2. We employ symmetry relations for the Fourier components of the reflection matrix [*de Haan et al.*, 1987; *Mishchenko*, 1990]. This saves nearly 50% of CPU time.

3. Since circular polarization, or the Stokes parameter V of the reflected sunlight, is typically negligible, all multiple-scattering computations are performed using the so-called (3×3) approximation which assumes neglecting the fourth column and the fourth row of the reflection and phase

Table 1. Expansion Coefficients for Rayleigh Scattering

s	a_1^s	a_2^s	a_3^s	a_4^s	b_1^s	b_2^s
0	1	0	0	0	0	0
1	0	0	0	$3d/2$	0	0
2	$c/2$	$3c$	0	0	$(3/2)^{1/2}c$	0

matrices appearing in equation (15) [*Hansen*, 1971]. Our extensive checks have shown that the computational accuracy of the (3×3) approximation is much higher than the expected accuracy of EOSP radiance and polarization measurements.

4. The zeroth Fourier component of the reflection matrix is computed using only the upper left (2×2) submatrices of the reflection and phase matrices [*Mishchenko*, 1990].

5. We diagonalize the matrices $\boldsymbol{P}_m^s(u)$ and use the supermatrix approach as described by *de Haan et al.* [1987].

6. We employ the analytical separation of the first-order aerosol scattering and the first-order surface reflection. The separation of the first-order aerosol scattering is described in detail by *de Haan et al.* [1987, p. 385]. The first-order surface reflection separation is an analogous procedure. Specifically, equation (12) is rewritten in the form

$$\boldsymbol{R}(\mu,\mu_0,\varphi-\varphi_0)=\boldsymbol{R}_0(\mu,\mu_0,\varphi-\varphi_0)\exp\left[-\tau_0\left(\frac{1}{\mu}+\frac{1}{\mu_0}\right)\right]$$
$$+\frac{1}{4}\sum_{m=0}^{M_1}(2-\delta_{m0})\left\{\left[(\boldsymbol{E}+\boldsymbol{D})\boldsymbol{\rho}^m(\tau_0;\mu,\mu_0)(\boldsymbol{E}+\boldsymbol{D})\right.\right.$$
$$+(\boldsymbol{E}-\boldsymbol{D})\boldsymbol{\rho}^m(\tau_0;\mu,\mu_0)(\boldsymbol{E}-\boldsymbol{D})\Big]\cos m(\varphi-\varphi_0)$$
$$+\Big[(\boldsymbol{E}-\boldsymbol{D})\boldsymbol{\rho}^m(\tau_0;\mu,\mu_0)(\boldsymbol{E}+\boldsymbol{D})$$
$$\left.-(\boldsymbol{E}+\boldsymbol{D})\boldsymbol{\rho}^m(\tau_0;\mu,\mu_0)(\boldsymbol{E}-\boldsymbol{D})\Big]\sin m(\varphi-\varphi_0)\right\}, \quad (37)$$

where

$$\boldsymbol{\rho}^m(\tau_0;\mu,\mu_0)=\boldsymbol{R}^m(\tau_0;\mu,\mu_0)$$
$$-\boldsymbol{R}_0^m(\mu,\mu_0)\exp\left[-\tau_0\left(\frac{1}{\mu}+\frac{1}{\mu_0}\right)\right], \quad (38)$$

τ_0 is the total optical thickness of the atmosphere, and $M_1 \ll M$. Extensive numerical checks have shown that using equation (37) instead of equation (12) allows one to compute far fewer Fourier components of the reflection matrix and thus to save a significant fraction of CPU time. Also we have found that when interpolation is used to compute the reflection matrix of an atmosphere-ocean system at μ and μ_0 different from division points used in Gaussian numerical integration in equation (15), employing equation (37) allows a much smaller number of Gaussian division points. Indeed, the first term on the right-hand side of equation (37) can be easily computed analytically for any μ, μ_0, and $\varphi-\varphi_0$ using formulas of the appendix, and only the second term needs to be interpolated. Since this latter term does not include the first-order surface reflection contribution, it is a relatively smooth function of μ and μ_0, thus providing a high numerical accuracy of interpolation even for a sparse grid of Gaussian division points. This provides a considerable saving of CPU time, since the number of floating point operations needed to solve the invariant imbedding equation is proportional to the third power of the number of Gaussian division points.

Finally, we note that an alternative numerical scheme entirely based on the adding/doubling method is described by J. Chowdhary et al. (Incorporation of a rough ocean surface and semi-infinite water body in multiple-scattering computations of polarized light in an atmosphere-ocean system, to be submitted to *Journal of Quantitative Spectroscopy and Radiative Transfer*, 1997).

3. Single-Scattering Characteristics of Aerosol Particles

All numerical results discussed below have been computed assuming the spherical particle shape and using the standard gamma distribution of particle radii given by [*Hansen and Travis*, 1974]

$$n(r) = C\, r^{\frac{1-3b}{b}} \exp\left(-\frac{r}{ab}\right), \quad (39)$$

where $n(r)dr$ is the fraction of particles with radii from r to $r + dr$, a and b are formal model parameters, and C is a constant which ensures the normalization

$$\int_0^\infty dr\, n(r) = 1 \quad (40)$$

and is equal to

$$C = \frac{1}{\Gamma\left(\frac{1-2b}{b}\right)}(ab)^{\frac{2b-1}{b}}. \quad (41)$$

For this distribution, the formal parameters a and b coincide with the cross-sectional-area weighted effective radius, r_{eff}, and the effective variance, v_{eff}, of the distribution, respectively, so that

$$a \equiv r_{\text{eff}} = \frac{1}{G}\int_0^\infty dr\pi r^3 n(r), \quad (42)$$

$$b \equiv v_{\text{eff}} = \frac{1}{Gr_{\text{eff}}^2}\int_0^\infty dr\left(r-r_{\text{eff}}\right)^2\pi r^2 n(r), \quad (43)$$

where

$$G = \int_0^\infty dr\pi r^2 n(r) \quad (44)$$

is the average particle geometric cross-sectional area. *Hansen and Travis* [1974] (see also *Hansen and Hovenier* [1974] and *Lacis et al.* [1992]) have shown that different size distributions of spherical particles having the same effective radius and effective variance have essentially identical scattering properties. Recently, *Mishchenko and Travis* [1994] have extended this result to polydispersions of randomly oriented spheroids. The results argue for a unified light-scattering classification of different size distributions based on only two key parameters and, in view of equations (42) and (43), make the gamma distribution especially convenient in theoretical computations. An additional

advantage of this distribution is that its moments are given by a simple formula [*Lacis and Mishchenko*, 1995]:

$$\langle r^n \rangle = \int_0^\infty dr\, r^n n(r)$$

$$= (ab)^n \Gamma[(1-2b)/b + n]/\Gamma[(1-2b)/b]$$

$$= a^n \prod_{j=1}^{n} [1 + (n-j-2)b]. \quad (45)$$

Throughout the paper, we use a fixed effective variance value $v_{\text{eff}} = 0.2$ corresponding to a moderately wide size distribution. Lognormal distributions for some "standard" aerosol models [e.g., *d'Almeida et al.*, 1991] often have (much) larger effective variances. However, as noted by *Lacis and Mishchenko* [1995], a problem in using very broad lognormal distributions is that they exhibit a physically unrealistic dependence on "phantom" 10 to 100-μm size particles that are implicitly contained within the large-particle tail of the distribution. Therefore it is preferable to describe a natural size distribution as a superposition of moderately broad-sized modes rather than to try to fit the in situ measured aerosol size spectrum with a single and implicitly broad-sized analytical distribution function and then to implicitly extrapolate it beyond the region of experimentally measured radii, thereby producing unrealistic results.

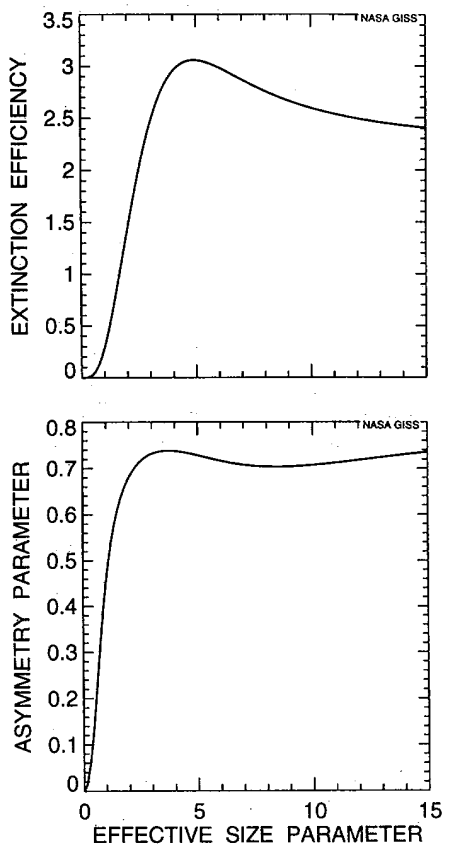

Figure 3. Extinction efficiency factor Q_{ext} and asymmetry parameter of the phase function g versus effective size parameter for a gamma distribution of spherical particles with effective variance $v_{\text{eff}} = 0.2$ and refractive index $m = 1.45$.

We have used the standard Mie theory [*van de Hulst*, 1957; *Hansen and Travis*, 1974; *de Rooij and van der Stap*, 1984] to compute the single-scattering properties of polydisperse spherical particles for a range of effective radii and refractive indices relevant to terrestrial tropospheric aerosols. Figure 3 shows the efficiency factor for extinction, Q_{ext}, and the asymmetry parameter of the phase function, g, versus effective size parameter $x_{\text{eff}} = 2\pi r_{\text{eff}}/\lambda$ for the particle refractive index $m = 1.45$, while Plate 1 demonstrates the variability of the extinction cross section C_{ext} and the asymmetry parameter with refractive index. The efficiency factor for extinction is defined as

$$Q_{\text{ext}} = \frac{C_{\text{ext}}}{G}, \quad (46)$$

where G is the average geometric cross-sectional area given by equation (44) and, for $v_{\text{eff}} = 0.2$, equal to

$$G = \pi \langle r^2 \rangle = \pi r_{\text{eff}}^2 (1 - v_{\text{eff}})(1 - 2v_{\text{eff}}) = 0.48\, \pi r_{\text{eff}}^2 \quad (47)$$

(cf. equation (45)). The asymmetry parameter of the phase function is given by

$$g = \frac{1}{2} \int_{-1}^{1} d(\cos\Theta)\, a_1(\Theta) \cos\Theta = \frac{a_1^1}{3}. \quad (48)$$

Plate 2 shows the scattering phase function $a_1(\Theta)$ versus scattering angle and effective size parameter for refractive indices varying from 1.3 to 1.7. Analogously, Plate 3 shows the quantity $-b_1(\Theta)/a_1(\Theta)$ (%), which is traditionally called the degree of linear polarization for single scattering of unpolarized incident light, and Plate 4 shows the ratio $a_3(\Theta)/a_1(\Theta)$ (%). Note that for spherical particles, $a_2(\Theta) \equiv a_1(\Theta)$ and $a_4(\Theta) \equiv a_3(\Theta)$. We do not display the scattering matrix element $b_2(\Theta)$, since its influence on the Stokes parameters I, Q, and U of the reflected sunlight is extremely weak and is explicitly neglected by using the (3×3) approximation. Since all computations have been performed for a zero imaginary part of the refractive index, the scattering cross section is equal to the extinction cross section and the single-scattering albedo w is equal to 1.

Comparison of Plates 1-4 shows that the asymmetry parameter of the phase function is least sensitive to aerosol refractive index so that the ratio $g(x_{\text{eff}}; m)/g(x_{\text{eff}}; 1.45)$ for $m \in [1.3; 1.7]$ and $x_{\text{eff}} \in [0; 15]$ does not deviate from 1 by more than ±25%. The extinction cross section ratio $C_{\text{sca}}(x_{\text{eff}}; m)/C_{\text{sca}}(x_{\text{eff}}; 1.45)$ can be as large as almost 2.5 and as small as 0.4 for effective size parameters about 1. However, for $x_{\text{eff}} \geq 6$ its deviation from 1 does not exceed ±10%, thus indicating that the theoretical diffraction limit [*van de Hulst*, 1957; *Bohren and Huffman*, 1983]

$$\lim_{x_{\text{eff}} \to \infty} \frac{C_{\text{ext}}(x_{\text{eff}}; m_1)}{C_{\text{ext}}(x_{\text{eff}}; m_2)} = 1 \quad (49)$$

is reached at relatively small effective size parameters.

The contour lines in the diagrams of Plate 2 are mostly vertical, thus showing a relatively weak variability of the scattering phase function with effective size parameter for

$x_{eff} \gtrsim 3$. The exception is the diffraction forward-scattering peak whose magnitude sharply increases with increasing x_{eff}. The dependence of $a_1(\Theta)$ on refractive index is also weak, especially at forward- and near-forward-scattering angles. The substantial rise of intensity at backscattering angles with increasing refractive index is explained by intensifying glory [*Hansen and Travis*, 1974]. Another effect of increasing refractive index is to make the side-scattering minimum at around $\Theta = 120°$ somewhat shallower.

Plate 3 clearly demonstrates that the single-scattering linear polarization $-b_1(\Theta)/a_1(\Theta)$ is the most sensitive function of aerosol refractive index and effective size parameter. With changing m and x_{eff}, polarization can change not only its magnitude, but even the sign. Even the region of Rayleigh scattering (i.e., the region of strong positive polarization occurring for the smallest size parameters) exhibits strong sensitivity to m and becomes more compressed with increasing refractive index. Given the expected very high accuracy of EOSP polarization measurements (±0.2% or even better), Plate 3 illustrates why polarimetry is potentially capable of discriminating between particles with very similar microphysical characteristics.

Plate 4 shows that although the ratio $a_3(\Theta)/a_1(\Theta)$ is less sensitive to aerosol refractive index and effective size parameter than the single-scattering linear polarization, it still shows a significant degree of variability with m and x_{eff}, especially at side-scattering and backscattering angles. Since the (3,3) element of the scattering matrix does not affect the polarization state of the first-order-scattering contribution to the sunlight reflected by an atmosphere, its remote sensing value has often been underestimated. However, we will show in the following section that even for optically thin atmospheres the multiple-scattering component of the reflected light is significant enough to make the (3,3) element a very important contributor to the power of polarimetry as a remote sensing tool.

4. Simulation of Aerosol Retrievals

The EOSP instrument will measure the reflectance, i.e., $\mu_0 R_{11}(\mu,\mu_0,\varphi-\varphi_0)$, and the Stokes parameter ratios Q/I and U/I or, equivalently, the reflection matrix ratios R_{21}/R_{11} and R_{31}/R_{11}. For conciseness, we will denote these three quantities as I, q, and u, respectively. We remind that, by definition, both q and u are measured with respect to the local meridian plane of the reflected beam.

To theoretically model satellite aerosol retrievals over the ocean, we have precomputed the quantities I, q, and u for a large set of "candidate" atmosphere-ocean models assuming a monomodal aerosol component with effective radius r_{eff} varying from 0 to 0.8 μm in steps of 0.01 μm, refractive index m varying from 1.3 to 1.7 in steps of 0.01, and aerosol optical thickness τ_0 ranging from 0 to 0.4 in steps of 0.01. Aerosol particles were assumed to be homogeneous spheres. All computations have been performed at a single and relatively long wavelength of $\lambda = 0.865$ μm, at which the contributions of light scattering in the ocean body and Rayleigh scattering in the atmosphere are negligible. Since the long-term annual mean wind speed just above the ocean surface varies from about 5 to about 9 m/s [*Hsiung*, 1986], we have used the mean square surface slope value $s^2 = 0.02$, roughly corresponding to a median wind speed of $W = 7$ m/s (cf. equation (18)). For this wind speed, the reflectance contribution due to oceanic whitecaps is negligibly small [*Koepke*, 1984].

First, we modeled the advanced very high resolution radiometer (AVHRR) type of aerosol retrievals [*Rao et al.*, 1989] by assuming that reflectance and/or polarization measurements of a scene are acquired at only one viewing angle. Also we assumed that the aerosol refractive index is known beforehand and is equal to 1.45, so that only the aerosol optical thickness and effective radius must be retrieved from the measurements. As computer-simulated measurement data, we chose the theoretically computed quantities I, q, and u for four "standard" models (hereafter referred to as the standard models (a), (b), (c), and (d)) with $\tau_0 = 0.2$ and $r_{eff} = 0.1$ μm (model (a)), 0.3 μm (model (b)), 0.5 μm (model (c)), and 0.7 μm (model (d)). The illumination and viewing geometries were specified by the values $\mu_0 = 0.8$, $\mu = 0.6$, and $\varphi - \varphi_0 = 60°$, so that the scattering angle was close to 103.9° (Figure 4). We then attempted to reconstruct the "unknown" optical thickness and effective radius for each of the four standard models by comparing their reflectivity and polarization with those for each of the candidate models from the large precomputed set. We have used three acceptance criteria which were designed to model retrievals using radiance only, polarization only,

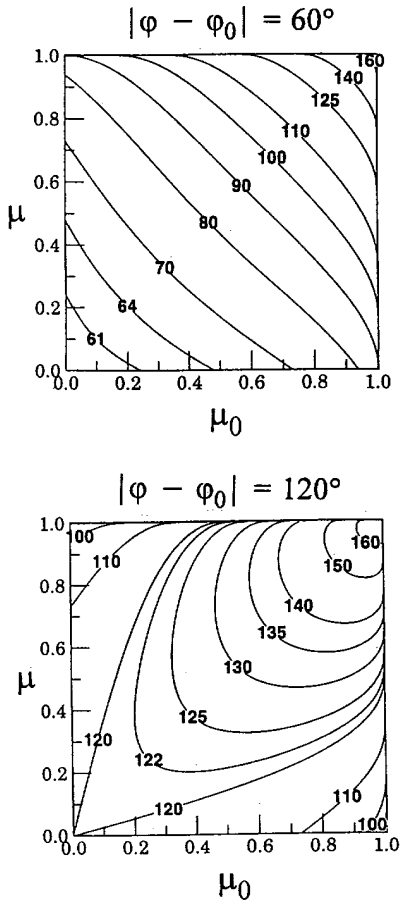

Figure 4. Scattering angle Θ versus μ and μ_0 for $|\varphi - \varphi_0| = 60°$ and 120°.

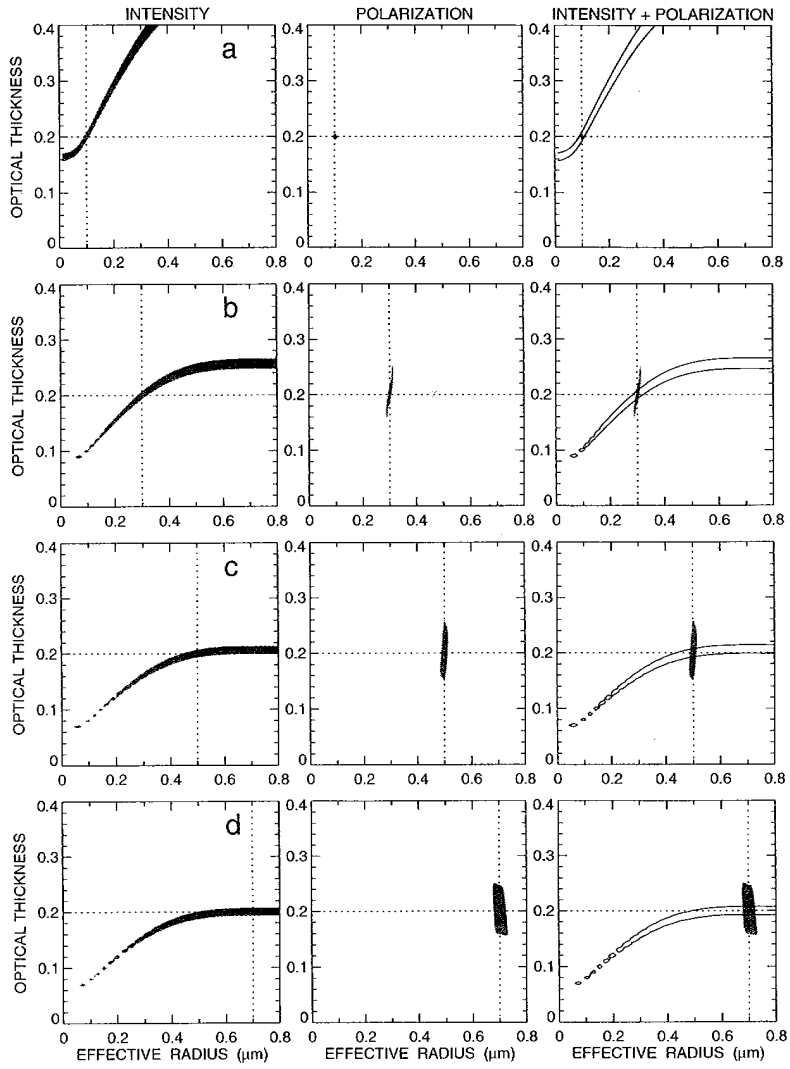

Figure 5. Modeling AVHRR-type aerosol optical thickness and effective radius retrievals using the reflectance-only (left panels), polarization-only (middle panels), and reflectance+polarization (right panels) acceptance criteria of equations (50)-(52) for four standard models with $\tau_0 = 0.2$ and r_{eff} = (a) 0.1 μm, (b) 0.3 μm, (c) 0.5 μm, and (d) 0.7 μm. The aerosol refractive index is assumed to be known beforehand ($m = 1.45$). The illumination and viewing geometries are specified by the values $\mu_0 = 0.8$, $\mu = 0.6$, and $\varphi - \varphi_0 = 60°$.

and radiance and polarization combined. The first two criteria, A and B, are given by

$$\frac{|I_c - I_s|}{I_s} \le 0.04 \qquad (50)$$

and

$$\frac{1}{2}\left(|q_c - q_s| + |u_c - u_s|\right) \le 0.002, \qquad (51)$$

respectively, while the third criterion, C, is a superposition of criteria A and B:

$$(C) = (A) \wedge (B). \qquad (52)$$

In equations (50) and (51), the indices s and c label quantities pertaining to standard and candidate models, respectively, and the right-hand sides of the criteria reflect the anticipated accuracy of EOSP reflectance and polarization measurements for typical aerosol optical thicknesses over the relatively dark ocean surface. The vertical and horizontal dotted lines in the panels of Figure 5 show the actual values of the optical thickness ($\tau_0 = 0.2$) and effective radius (r_{eff} = 0.1, 0.3, 0.5, and 0.7 μm) for the four standard models so that the intersection of the lines indicates the correct solution. In the leftmost set of panels, the shadowed areas show the candidate models that passed the radiance-only criterion A. Similarly, the middle panels show the result of applying the polarization-only criterion B, while the panels on the right show the intersections of the shadowed areas from the left and middle panels and demonstrate the result of criterion C based on the simultaneous use of reflectance and polarization measurements. It is clearly seen that reflectance measurements alone cannot be used to reconstruct both unknown parameters (τ_0 and r_{eff}) and that assuming a wrong

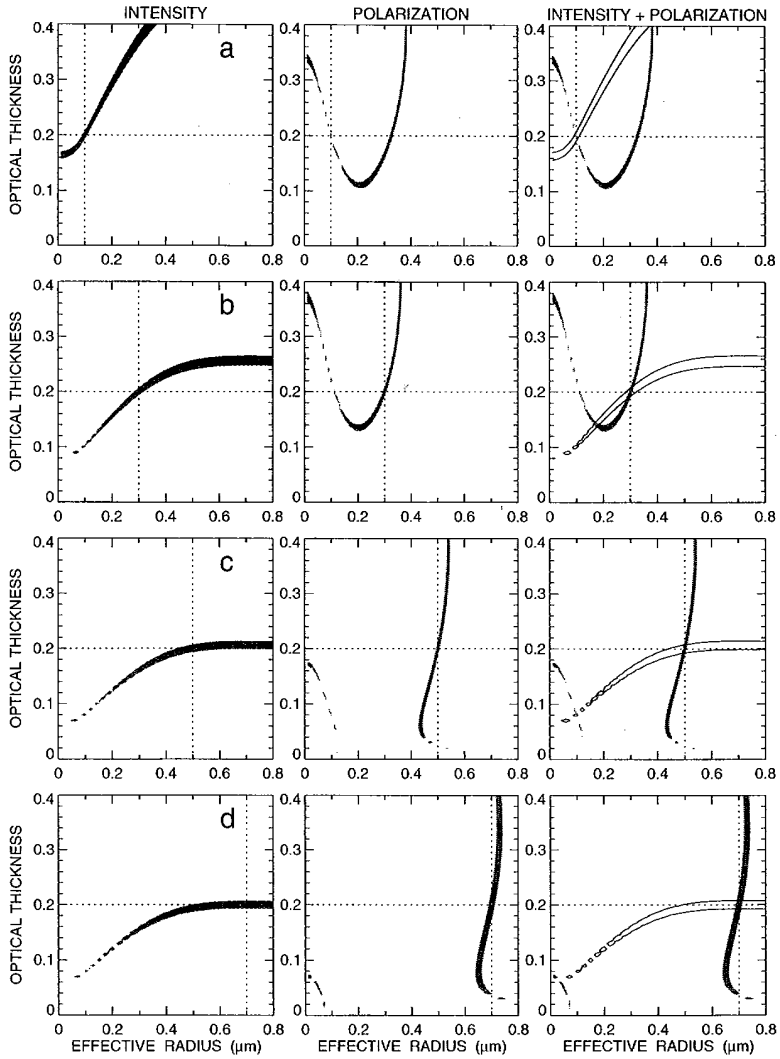

Figure 6. As in Figure 5, except using the modified polarization-only criterion given by equation (58).

effective radius can result in a very large error in the retrieved optical thickness, especially for standard model (a), and vice versa. This conclusion is in full agreement with findings of *Wang and Gordon* [1994]. The middle panels show that polarization alone is doing a better job in proving narrower constraints on the unknown parameters τ_0 and r_{eff}. This is not surprising, since criterion B is based on measuring two quantities (q and u), whereas criterion A is based on measuring only reflectance I. Combined use of reflectance and polarization measurements shown in the panels on the right (Figure 5) provides an almost perfect retrieval of both the optical thickness and the effective radius.

It has often been stated that the high sensitivity of polarimetry to particle characteristics is partly explained by the fact that most of the remote sensing polarization signature comes from the first-order scattering in the atmosphere. Our calculations show, however, that this can be a slightly misleading oversimplification. The first-order-scattering contributions to the (2,1) and (3,1) elements of the reflection matrix for an atmosphere of optical thickness τ_0 above a fully absorbing surface are given by

$$R_{21}^{(1)}(\mu,\mu_0,\varphi-\varphi_0)=CZ_{21}(-\mu,\mu_0,\varphi-\varphi_0)$$
$$=Cb_1(\Theta)\cos 2\sigma_2 \tag{53}$$

and

$$R_{31}^{(1)}(\mu,\mu_0,\varphi-\varphi_0)=CZ_{31}(-\mu,\mu_0,\varphi-\varphi_0)$$
$$=-Cb_1(\Theta)\sin 2\sigma_2, \tag{54}$$

where

$$C=\frac{w}{4(\mu+\mu_0)}\left\{1-\exp\left[-\left(\frac{1}{\mu}+\frac{1}{\mu_0}\right)\tau_0\right]\right\} \tag{55}$$

(cf. equation (31) and Figure 2). Thus, these two contributions are not independent but are rather proportional to each other:

$$R_{31}^{(1)}(\mu,\mu_0,\varphi-\varphi_0)=-R_{21}^{(1)}(\mu,\mu_0,\varphi-\varphi_0)\tan\sigma_2. \tag{56}$$

So if the remote sensing content of polarization were

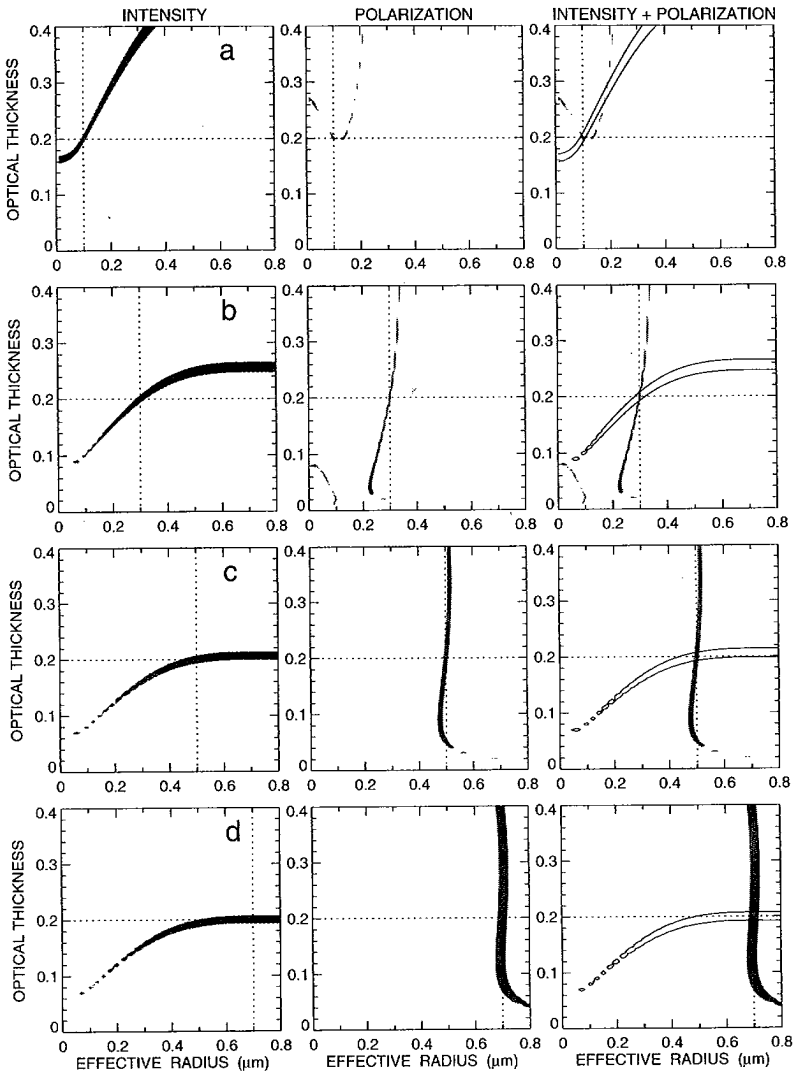

Figure 7. As in Figure 5, except using the modified polarization-only criterion given by equation (59).

dominated by first-order scattering, the measured quantities q and u would not be two independent pieces of information. Rather, the polarization plane (i.e., the plane through the beam and the major axis of the polarization ellipse [*Hovenier and van der Mee*, 1983] would always be precisely parallel or perpendicular to the scattering plane, and the only quantitative information content of polarization would come from the degree of linear polarization defined as

$$P = \left(q^2 + u^2\right)^{1/2}. \tag{57}$$

Figures 6 and 7 are analogous to Figure 5 except that instead of criterion B given by equation (51), they use the polarization-only criteria

$$|q_c - q_s| \leq 0.002 \tag{58}$$

or

$$|P_c - P_s| \leq 0.002, \tag{59}$$

respectively. It is obvious that the performance of these modified polarization criteria based on only one Stokes parameter or only on the degree of linear polarization is much worse than that of the original criterion employing u as well as q. Furthermore, even the combined use of intensity and polarization (rightmost panels of Figures 6 and 7) does not eliminate multiple solutions (cf. corresponding panels of Figure 5). This means that an important effect of multiple scattering is to bring to play the (3,3) element of the scattering matrix $a_3(\Theta)$, thus making q and u independent pieces of information and providing a much better constraint on aerosol characteristics if the measured Stokes parameters are sufficiently accurate. Equivalently, it is apparent that the quantitative remote sensing content of polarization comes not only from the degree of linear polarization P but also from the deviation of the polarization plane orientation from the parallel or perpendicular orientation with respect to the scattering plane. We must therefore conclude that the full remote sensing potential of polarimetry is realized only when this deviation of polarization plane orientation is explicitly treated using measurements with sufficient accuracy to be sensitive enough to detect the deviation.

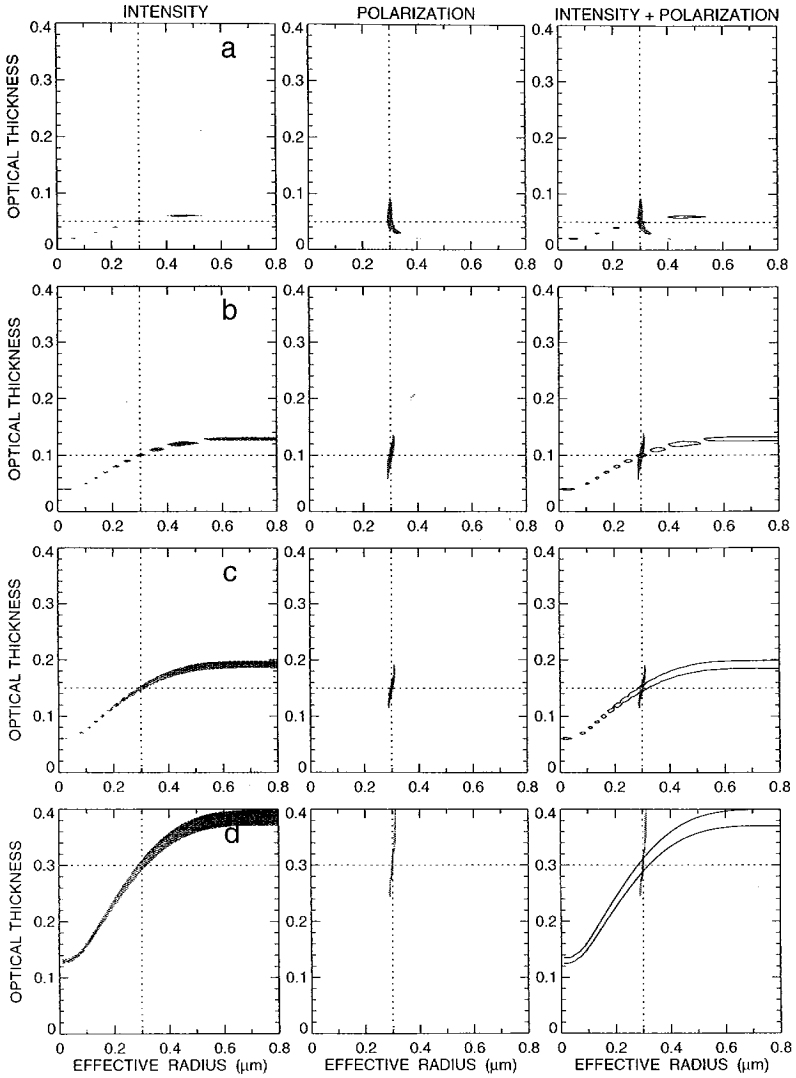

Figure 8. As in Figure 5, except for standard models with r_{eff} = 0.4 μm and τ_0 = (a) 0.05, (b) 0.1, (c) 0.15, and (d) 0.3.

Figure 8 is analogous to Figure 5 but is computed for four new standard models having the same effective radius r_{eff} = 0.4 μm and optical thicknesses τ_0 = 0.05 (model (a)), 0.1 (model (b)), 0.15 (model (c)), and 0.3 (model (d)), and we revert to the criterion B of equation (51). Again, the aerosol refrective index is assumed to be known (m = 1.45), so that only r_{eff} and τ_0 need be retrieved. One sees that in all cases, polarization is much more sensitive to the aerosol effective radius and that the combined use of radiance and polarization provides an almost perfect solution.

Figure 9 shows results for the same standard models as Figure 5 but for a different viewing angle given by the cosine of the satellite zenith angle μ = 0.6 and the relative satellite-Sun azimuth angle $\varphi - \varphi_0 = -120°$. For this scattering geometry, the scattering angle is close to Θ = 136° (cf. Figure 4). Again, in the case of the standard models (b), (c), and (d) the sensitivities of reflectance and polarization are nearly orthogonal and their combined use produces an almost perfect solution for both "unknown" parameters τ_0 and r_{eff}. However, for the standard model (a), multiple solutions are possible even if both reflectance and polarization are used simultaneously. In this case, additional information such as observations at additional viewing angles is needed to find a unique solution for both r_{eff} and τ_0.

Figure 10 differs from Figure 5 in that it assumes that the aerosol effective radius is known a priori and is r_{eff} = 0.4 μm, and uses four standard models having the same optical thickness τ_0 = 0.2 and refractive indices m = 1.35 (model (a)), 1.45 (model (b)), 1.55 (model (c)), and 1.65 (model (d)). Figure 11 is similar but is computed for $\varphi - \varphi_0 = -120°$. These figures show again that reflectance measurements alone cannot be used to uniquely retrieve both unknown parameters (now, aerosol optical thickness and refractive index), that polarization is much more sensitive to the aerosol refractive index than to the optical thickness, and that the combined use of reflectance and polarization provides a nearly perfect retrieval of both τ_0 and m.

The second type of aerosol retrieval algorithms that we have modeled can be called the multi-angle imaging spectroradiometer (MISR)/EOSP type, since it uses multiple-

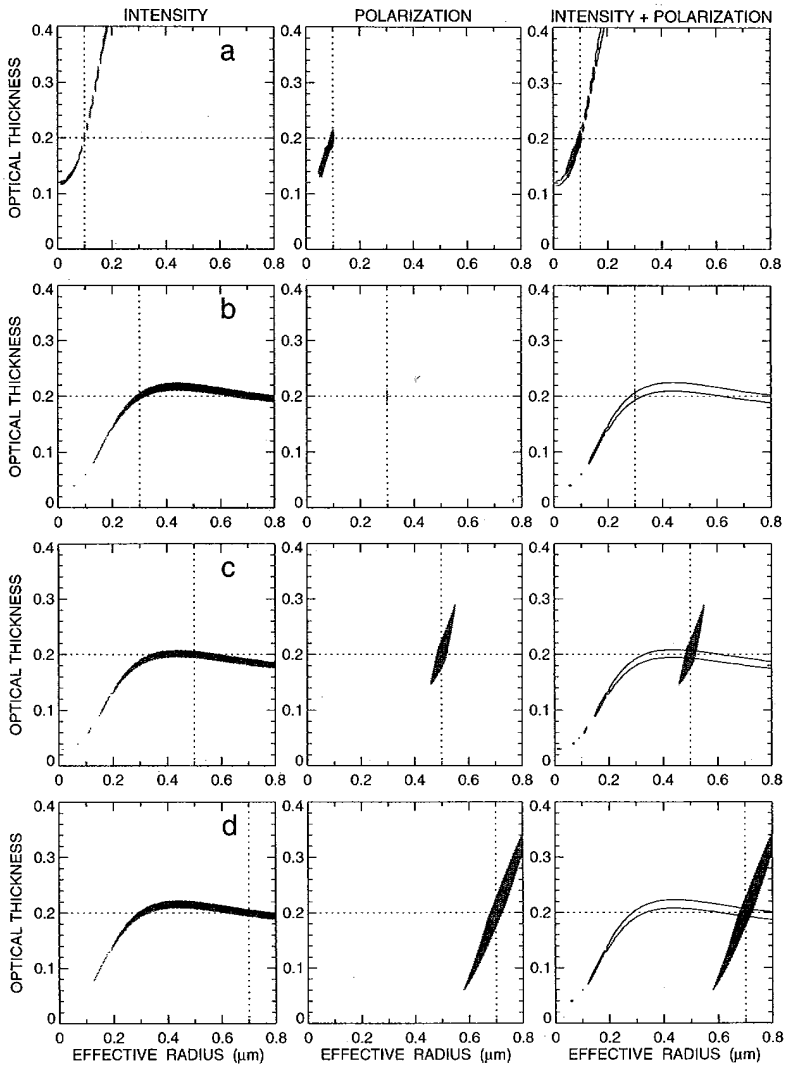

Figure 9. As in Figure 5, except for $\varphi - \varphi_0 = -120°$.

viewing-angle measurements of radiance and/or polarization for a given scene. Specifically, we have assumed that the cosine of the Sun zenith angle is fixed at $\mu_0 = 0.8$ and the cosine of the satellite zenith angles varies from $\mu = 0.2$ to 1 in steps of 0.2 in the satellite orbit plane given by the relative satellite-Sun azimuth angles $\varphi - \varphi_0 = 60°$ and $-120°$, so there are nine different viewing directions. This type of measurement covers the range of scattering angles from about 82° to 148° (Figure 4). We have modified the acceptance criteria of equations (50) and (51) so that now they specify the maximum allowable relative/absolute difference between the standard and candidate models averaged over the nine measurements:

$$\frac{1}{9}\sum_{j=1}^{9}\frac{|I_c^j - I_s^j|}{I_s^j} \le 0.04, \tag{60}$$

$$\frac{1}{9}\sum_{j=1}^{9}\frac{1}{2}\left(|q_c^j - q_s^j| + |u_c^j - u_s^j|\right) \le 0.002, \tag{61}$$

for criteria A and B, respectively, where the superscript j numbers the viewing directions. The intensity+polarization acceptance criterion is again the superposition of criteria A and B.

Figure 12 assumes that the aerosol refractive index is known a priori ($m = 1.45$) and models the retrieval of the aerosol optical thickness and effective radius for four standard aerosol models with $\tau_0 = 0.2$ and $r_{eff} = 0.1$ μm (model (a)), 0.2 μm (model (b)), 0.5 μm (model (c)), and 0.7 μm (model (d)). Similarly, Figure 13 assumes that the aerosol effective radius is known ($r_{eff} = 0.4$ μm) and models the retrieval of the aerosol optical thickness and refractive index for standard models with $\tau_0 = 0.2$ and $m = 1.35$ (model (a)), 1.45 (model (b)), 1.55 (model (c)), and 1.65 (model (d)). It is seen that the algorithm utilizing reflectances only (leftmost panels) now works much better than in the case of single-viewing-angle measurements. Nonetheless, its sensitivity to aerosol microphysics (r_{eff} and m) can be poor in some cases. For example, in the case of model (b) in Figure 12, the retrieved aerosol optical thickness can differ from the actual value by more than 0.1 or 50%. In contrast, the polarization-only algorithm (middle panels) is doing an

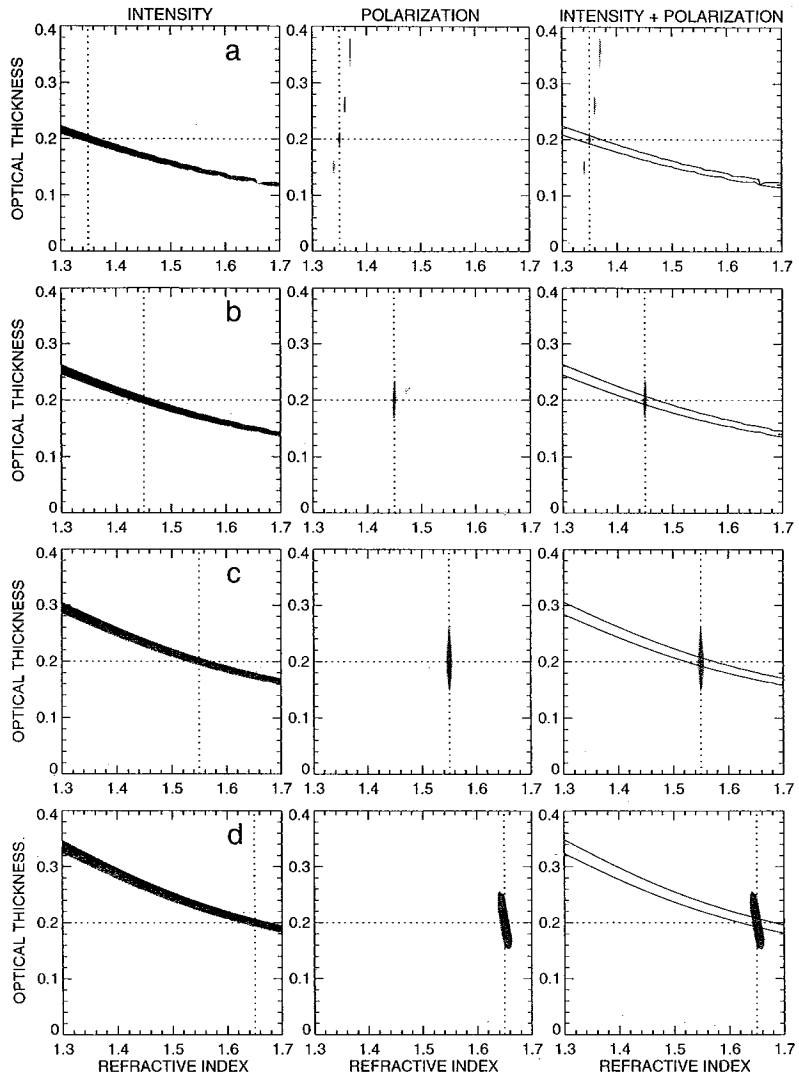

Figure 10. Modeling AVHRR-type aerosol optical thickness and refractive index retrievals using the acceptance criteria of equations (50)-(52) for four standard models with $\tau_0 = 0.2$ and $m =$ (a) 1.35, (b) 1.45, (c) 1.55, and (d) 1.65. The aerosol effective radius is assumed to be known beforehand ($r_{eff} = 0.4$ μm). The illumination and viewing geometries are specified by the values $\mu_0 = 0.8$, $\mu = 0.6$, and $\varphi - \varphi_0 = 60°$.

excellent job and in all cases provides a nearly perfect solution, especially for r_{eff} and m. Moreover, the simultaneous use of radiance and polarization measurements further improves the optical thickness estimate, making the absolute accuracy of the τ_0 retrieval better than 0.01 (rightmost panels). Note that we have omitted dotted lines in some of the panels of Figure 12 in order not to overwrite the extremely narrow regions of possible solutions retrieved with the polarization-only algorithm.

The most stringent test of the three MISR/EOSP type algorithms (radiance alone, polarization alone, and radiance+polarization) would be to assume that all three model parameters (τ_0, r_{eff}, m) are unknown and need to be retrieved without using any a priori information. As a standard model for this test, we have chosen aerosols having $\tau_0 = 0.2$, $r_{eff} = 0.4$ μm, and $m = 1.45$. Figure 14 demonstrates the performance of the three algorithms by displaying results for candidate model optical thicknesses varying from 0 to 0.4, refractive indices varying from 1.3 to 1.7, and effective radii ranging from 0.2 to 0.7 μm. Our computations show that the polarization-only algorithm alone provides an almost perfect retrieval of the aerosol optical thickness and refractive index and constrains the effective radius to within ±0.03 μm. The fit for polarization is so restrictive that all the middle panels but one have no shadowed areas corresponding to acceptable models. We even had to omit the dotted lines in many panels in order to clearly show the absence of acceptable solutions and the extremely small size of the shadowed area obtained with the polarization-only criterion. The use of radiance in addition to polarization slightly improves the accuracy of the aerosol optical thickness retrieval to ±0.01. In contrast, the radiance-only algorithm is capable of producing wrong solutions, with all three retrieved model parameters deviating significantly

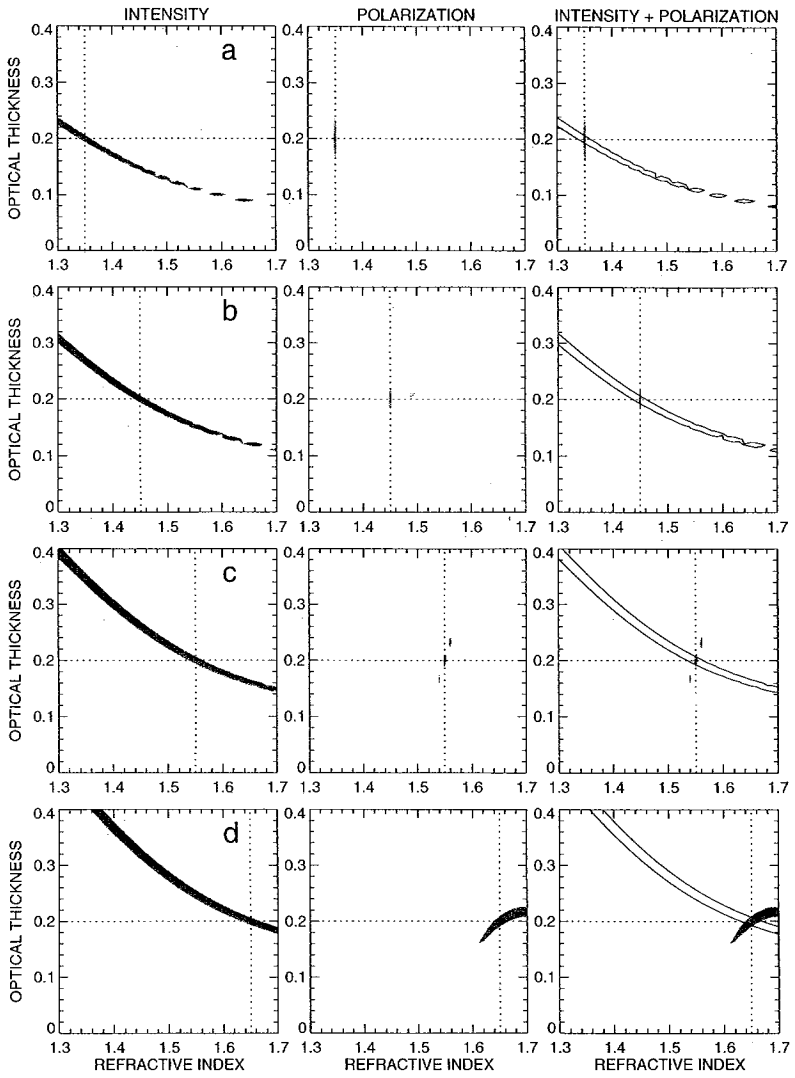

Figure 11. As in Figure 10, except for $\varphi - \varphi_0 = -120°$.

from actual values. The error in the retrieved optical thickness can exceed 0.1 or 50%; the error in the retrieved effective radius can be as large as 0.3 μm (75%); and the error in the retrieved refractive index can be larger than 0.1.

5. Discussion and Conclusions

In this paper, we have used numerically accurate solutions of the vector radiative transfer equation for a realistic atmosphere-ocean model to theoretically simulate several types of satellite aerosol retrievals over the ocean. Specifically, we have simulated what can be called the AVHRR and MISR/EOSP types of measurements with one and several observation directions for a scene, respectively, and algorithms utilizing radiance measurements only, polarization measurements only, and radiance and polarization measurements combined. We have restricted all simulations to a single near-infrared wavelength of 0.865 μm and, accordingly, used a relatively simple atmosphere-ocean model with no contributions to the reflectance due to scattering from within the ocean body or from Rayleigh scattering by molecules of the atmosphere. Also, we have assumed that aerosols are spherical, single-component, monomodal, and nonabsorbing. These simplifications allow us to test the various algorithms under exactly the same conditions with a practical computational level of effort and thus examine their relative strengths and weaknesses for circumstances reasonably representative of natural conditions.

Figures 5 and 8-11 [see also *Wang and Gordon*, 1994] clearly demonstrate the limitations in the performance that can be expected from an AVHRR-type aerosol retrieval algorithm utilizing only one reflectance measurement of a scene at a single wavelength and for a single observation geometry. Our computations fully corroborate the conclusion of *Diner et al.* [1994] that the reported AVHRR sensitivity to optical thickness (RMS error) of about 0.04 does not necessarily provide a measure of accuracy because it does not include systematic biases due to the particular model assumed in the retrieval. As Figure 11 demonstrates, even for spherical particles with a known size distribution, an error of

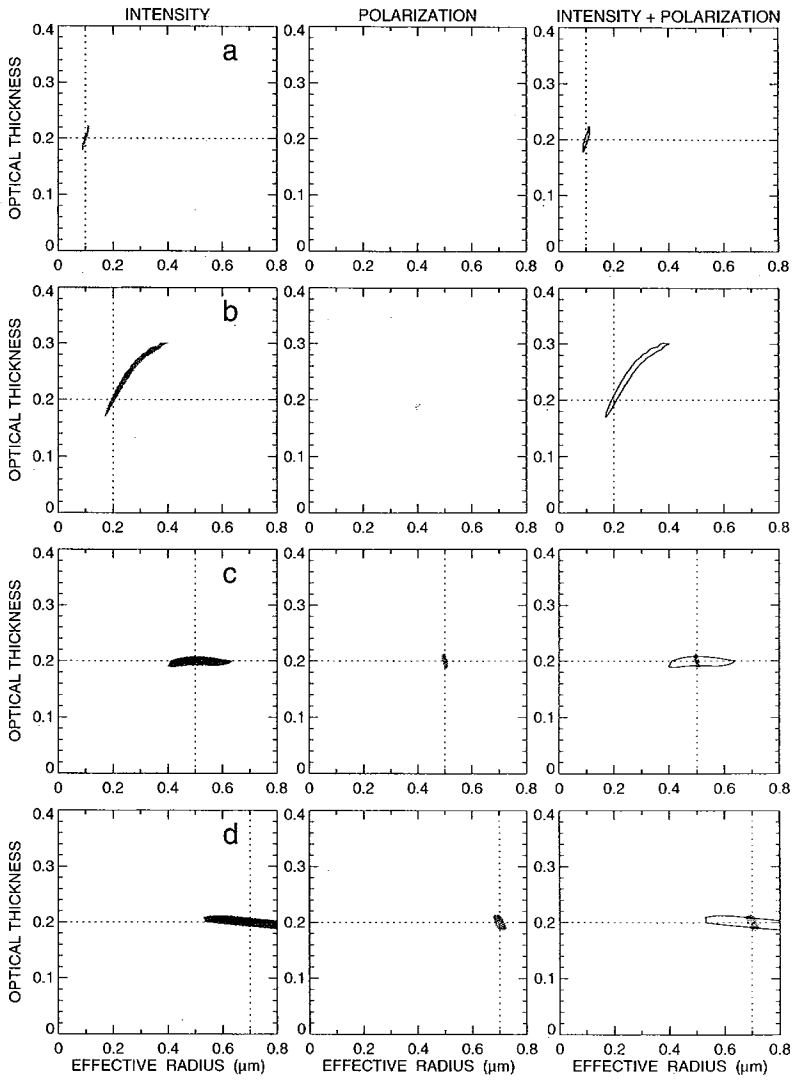

Figure 12. Modeling MISR/EOSP-type aerosol optical thickness and effective radius retrievals using the acceptance criteria of equations (60), (61), and (52) for four standard models with $\tau_0 = 0.2$ and r_{eff} = (a) 0.1 μm, (b) 0.2 μm, (c) 0.5 μm, and (d) 0.7 μm. The aerosol refractive index is assumed to be known beforehand ($m = 1.45$). The illumination and viewing geometries are specified by the values $\mu_0 = 0.8$; $\mu = 0.2$, 0.4, 0.6, 0.8, and 1; and $\varphi - \varphi_0 = 60°$ and $-120°$.

as much as a factor of 2 can occur in the retrieved aerosol optical thickness if an incorrect value is assumed for the real part of the refractive index. It is obvious that having only one piece of information, it is impossible to uniquely retrieve all three unknown model parameters (τ_0, r_{eff}, and m) and even any two of them.

Figures 12-14 demonstrate the advantage of the MISR strategy, which employs additional data in the form of radiance measurements taken at a number of observation angles in order to provide much narrower constraints on aerosol characteristics. However, even in this case, measurements at only one wavelength may not be sufficient to uniquely determine all three model parameters (aerosol optical thickness, effective radius, and refractive index) with high enough accuracy.

In contrast, our computations show that even for the AVHRR type of measurements, the combined use of radiance and high-precision polarization data can significantly ameliorate the uniqueness problem. Furthermore, in the case of the MISR/EOSP type of measurements, high-precision polarimetry alone is capable of uniquely retrieving all three model parameters with the level of accuracy needed for long-term monitoring of global climate forcings and feedbacks. The simultaneous use of radiance measurements in this case does not affect the accuracy of effective radius and refractive index retrievals, but slightly improves the accuracy of the optical thickness retrieval. An important conclusion that follows from our simulations is that the full remote sensing potential of polarimetry can only be realized if both Stokes parameter ratios Q/I and U/I are measured and used in the retrieval rather than only one of them or the degree of linear polarization P.

Of course, the performance of the moderate resolution imaging spectrometer (MODIS) and MISR instruments will

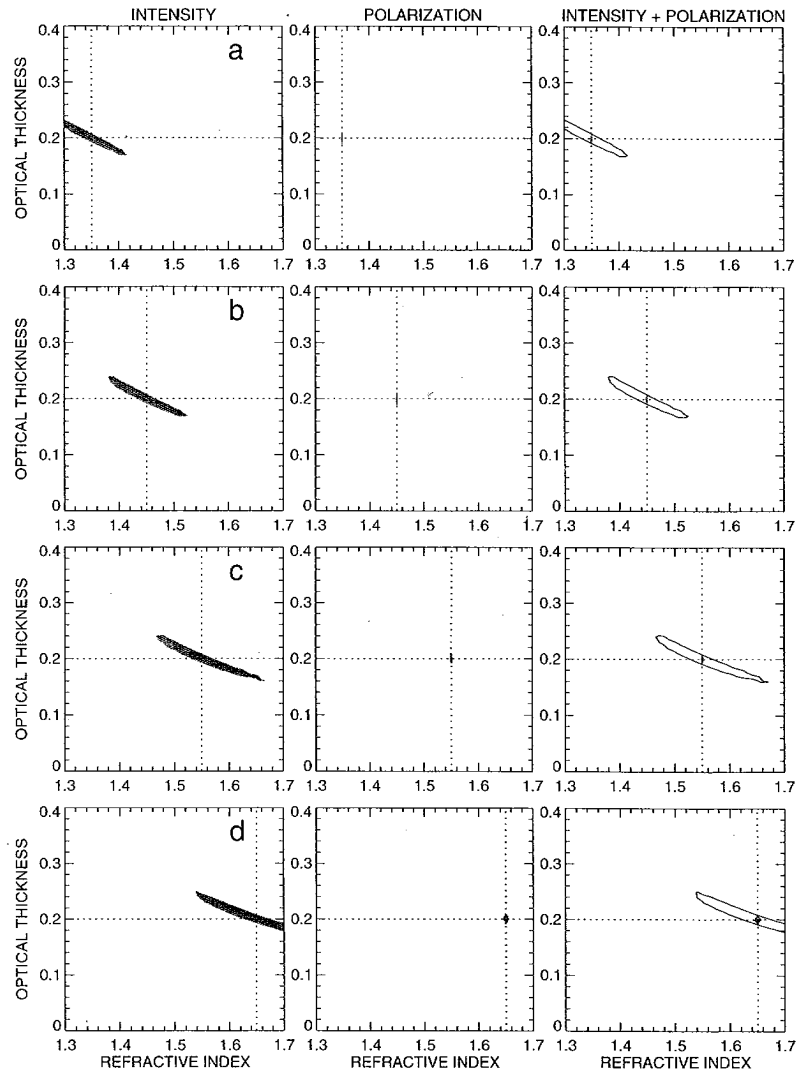

Figure 13. Modeling MISR/EOSP-type aerosol optical thickness and refractive index retrievals using the acceptance criteria of equations (60), (61), and (52) for four standard models with $\tau_0 = 0.2$ and m = (a) 1.35, (b) 1.45, (c) 1.55, and (d) 1.65. The aerosol effective radius is assumed to be known beforehand ($r_{\text{eff}} = 0.4$ μm). The illumination and viewing geometries are specified by the values $\mu_0 = 0.8$; $\mu = 0.2$, 0.4, 0.6, 0.8, and 1; and $\varphi - \varphi_0 = 60°$ and $-120°$.

be improved by utilizing multispectral measurements covering a relatively broad range of wavelengths. The multispectral information can be used to provide narrower constraints on aerosol characteristics, especially optical thickness and effective radius. However, the EOSP instrument will also provide high-accuracy multispectral radiance and polarization data, which can be used to retrieve parameters of a much more sophisticated model including multicomponent, multimodal, nonspherical, and/or absorbing aerosols. The present analysis strongly suggests that algorithms utilizing high-precision polarization as well as radiance measurements are much less dependent on the availability and use of a priori information and can be expected to provide a physically based retrieval of aerosol characteristics with extremely high accuracy. A theoretical examination of the performance of polarimetry in the case of more complicated aerosol models is under way.

Appendix: Reflection Matrix of a Rough Air-Water Interface

For directions of light incidence and reflection $\boldsymbol{n}_0 = (-\mu_0, \varphi_0)$ and $\boldsymbol{n} = (\mu, \varphi)$, respectively, the ocean reflection matrix in the Kirchhoff approximation is given by [*Tsang et al.*, 1985]

$$\boldsymbol{R}_o(\mu, \mu_0, \varphi - \varphi_0) = \frac{|\boldsymbol{k}_d|^4}{4\mu\mu_0 |\boldsymbol{n} \times \boldsymbol{n}_0|^4 k_{dz}^4 2s^2} \times \exp\left[-\frac{k_{dx}^2 + k_{dy}^2}{2k_{dz}^2 s^2}\right] \boldsymbol{M}(\mu, \mu_0, \varphi - \varphi_0), \quad (62)$$

where

$$\boldsymbol{k}_d = k[\boldsymbol{n}_0 - \boldsymbol{n}] = k_{dx}\boldsymbol{x} + k_{dy}\boldsymbol{y} + k_{dz}\boldsymbol{z}, \quad (63)$$

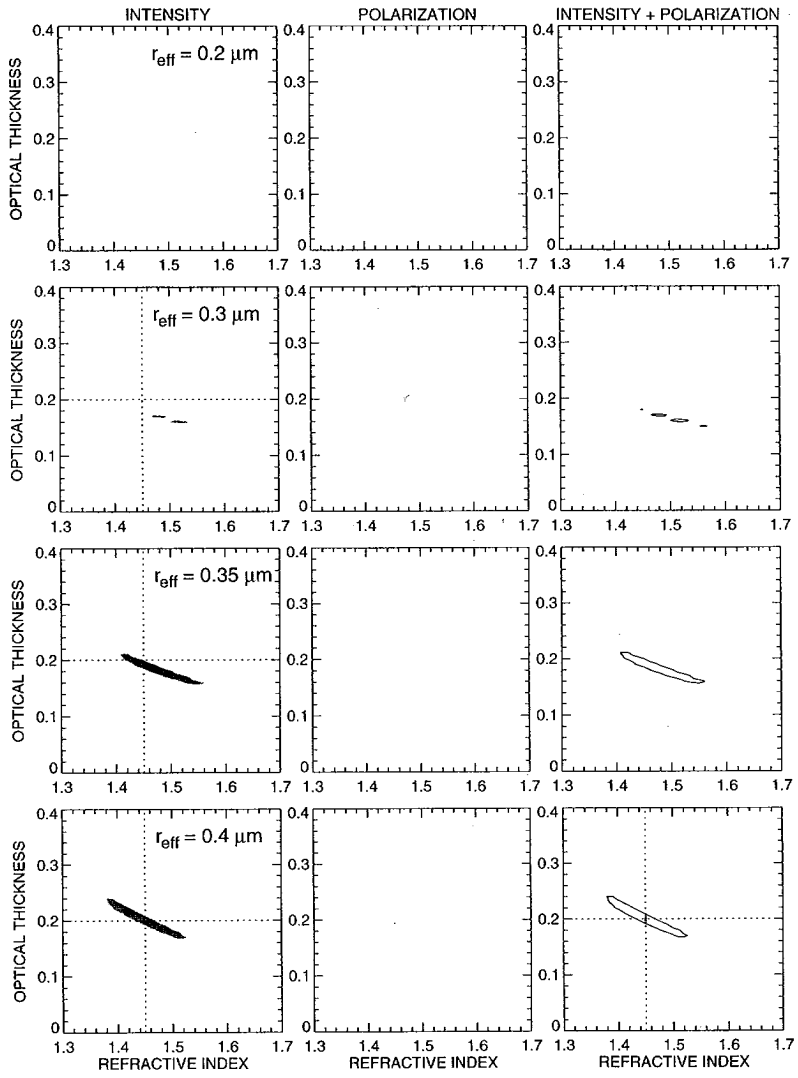

Figure 14a. Modeling MISR/EOSP-type aerosol optical thickness, effective radius, and refractive index retrievals using the acceptance criteria of equations (60), (61), and (52) for a standard model with $\tau_0 = 0.2$, $r_{eff} = 0.4$ μm, and $m = 1.45$. All three model parameters are assumed to be unknown. The illumination and viewing geometries are specified by the values $\mu_0 = 0.8$; $\mu = 0.2$, 0.4, 0.6, 0.8, and 1; and $\varphi - \varphi_0 = 60°$ and $-120°$. Calculations are shown for candidate aerosol model effective radii $r_{eff} = 0.2$, 0.3, 0.35, and 0.4 μm.

s^2 is the mean square surface slope, and $k = 2\pi/\lambda$ is the free-space wavenumber for the free-space wavelength λ. The elements of the (4×4) matrix $\boldsymbol{M}(\mu,\mu_0,\varphi-\varphi_0)$ are given by

$$M_{11} = \frac{1}{2}\left[|f_{\vartheta\vartheta}|^2 + |f_{\vartheta\varphi}|^2 + |f_{\varphi\vartheta}|^2 + |f_{\varphi\varphi}|^2\right], \quad (64)$$

$$M_{12} = \frac{1}{2}\left[|f_{\vartheta\vartheta}|^2 - |f_{\vartheta\varphi}|^2 + |f_{\varphi\vartheta}|^2 - |f_{\varphi\varphi}|^2\right], \quad (65)$$

$$M_{21} = \frac{1}{2}\left[|f_{\vartheta\vartheta}|^2 + |f_{\vartheta\varphi}|^2 - |f_{\varphi\vartheta}|^2 - |f_{\varphi\varphi}|^2\right], \quad (66)$$

$$M_{22} = \frac{1}{2}\left[|f_{\vartheta\vartheta}|^2 - |f_{\vartheta\varphi}|^2 - |f_{\varphi\vartheta}|^2 + |f_{\varphi\varphi}|^2\right], \quad (67)$$

$$M_{13} = -\mathrm{Re}\left[f_{\vartheta\vartheta} f_{\vartheta\varphi}^* + f_{\varphi\vartheta} f_{\varphi\varphi}^*\right], \quad (68)$$

$$M_{14} = -\mathrm{Im}\left[f_{\vartheta\vartheta} f_{\vartheta\varphi}^* + f_{\varphi\vartheta} f_{\varphi\varphi}^*\right], \quad (69)$$

$$M_{23} = -\mathrm{Re}\left[f_{\vartheta\vartheta} f_{\vartheta\varphi}^* - f_{\varphi\vartheta} f_{\varphi\varphi}^*\right], \quad (70)$$

$$M_{24} = -\mathrm{Im}\left[f_{\vartheta\vartheta} f_{\vartheta\varphi}^* - f_{\varphi\vartheta} f_{\varphi\varphi}^*\right], \quad (71)$$

$$M_{31} = -\mathrm{Re}\left[f_{\vartheta\vartheta} f_{\vartheta\vartheta}^* + f_{\vartheta\varphi} f_{\varphi\varphi}^*\right], \quad (72)$$

$$M_{32} = -\mathrm{Re}\left[f_{\vartheta\vartheta} f_{\vartheta\vartheta}^* - f_{\vartheta\varphi} f_{\varphi\varphi}^*\right], \quad (73)$$

$$M_{33} = \mathrm{Re}\left[f_{\vartheta\vartheta} f_{\varphi\varphi}^* + f_{\vartheta\varphi} f_{\varphi\vartheta}^*\right], \quad (74)$$

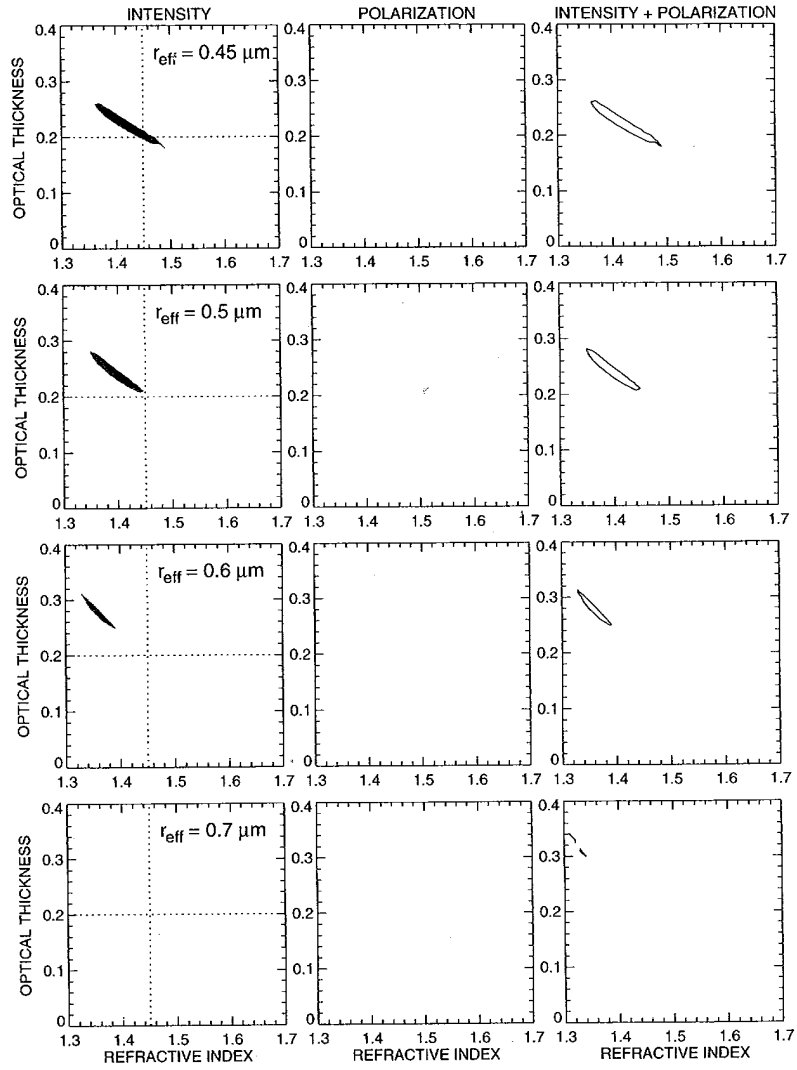

Figure 14b. As in Figure 14a, except for candidate aerosol model effective radii $r_{\text{eff}} = 0.45$, 0.5, 0.6, and 0.7 μm.

$$M_{34} = \text{Im}\left[f_{\vartheta\vartheta} f_{\varphi\varphi}^{*} - f_{\vartheta\varphi} f_{\varphi\vartheta}^{*}\right], \tag{75}$$

$$M_{41} = \text{Im}\left[f_{\vartheta\vartheta} f_{\varphi\vartheta}^{*} + f_{\vartheta\varphi} f_{\varphi\varphi}^{*}\right], \tag{76}$$

$$M_{42} = \text{Im}\left[f_{\vartheta\vartheta} f_{\varphi\vartheta}^{*} - f_{\vartheta\varphi} f_{\varphi\varphi}^{*}\right], \tag{77}$$

$$M_{43} = -\text{Im}\left[f_{\vartheta\vartheta} f_{\varphi\varphi}^{*} + f_{\vartheta\varphi} f_{\varphi\vartheta}^{*}\right], \tag{78}$$

$$M_{44} = \text{Re}\left[f_{\vartheta\vartheta} f_{\varphi\varphi}^{*} - f_{\vartheta\varphi} f_{\varphi\vartheta}^{*}\right], \tag{79}$$

where

$$f_{\vartheta\vartheta} = (\boldsymbol{\varphi}_0\cdot\boldsymbol{n})(\boldsymbol{\varphi}\cdot\boldsymbol{n}_0)R_{\perp} + (\boldsymbol{\vartheta}_0\cdot\boldsymbol{n})(\boldsymbol{\vartheta}\cdot\boldsymbol{n}_0)R_{\parallel}, \tag{80}$$

$$f_{\vartheta\varphi} = -(\boldsymbol{\vartheta}_0\cdot\boldsymbol{n})(\boldsymbol{\varphi}\cdot\boldsymbol{n}_0)R_{\perp} + (\boldsymbol{\varphi}_0\cdot\boldsymbol{n})(\boldsymbol{\vartheta}\cdot\boldsymbol{n}_0)R_{\parallel}, \tag{81}$$

$$f_{\varphi\vartheta} = -(\boldsymbol{\varphi}_0\cdot\boldsymbol{n})(\boldsymbol{\vartheta}\cdot\boldsymbol{n}_0)R_{\perp} + (\boldsymbol{\vartheta}_0\cdot\boldsymbol{n})(\boldsymbol{\varphi}\cdot\boldsymbol{n}_0)R_{\parallel}, \tag{82}$$

$$f_{\varphi\varphi} = (\boldsymbol{\vartheta}_0\cdot\boldsymbol{n})(\boldsymbol{\vartheta}\cdot\boldsymbol{n}_0)R_{\perp} + (\boldsymbol{\varphi}_0\cdot\boldsymbol{n})(\boldsymbol{\varphi}\cdot\boldsymbol{n}_0)R_{\parallel}, \tag{83}$$

$$R_{\perp} = \frac{\cos\theta - \sqrt{m^2 - 1 + \cos^2\theta}}{\cos\theta + \sqrt{m^2 - 1 + \cos^2\theta}}, \tag{84}$$

$$R_{\parallel} = \frac{m^2\cos\theta - \sqrt{m^2 - 1 + \cos^2\theta}}{m^2\cos\theta + \sqrt{m^2 - 1 + \cos^2\theta}}, \tag{85}$$

$$\cos\theta = -\frac{\boldsymbol{n}_0\cdot(\boldsymbol{n} - \boldsymbol{n}_0)}{|\boldsymbol{n} - \boldsymbol{n}_0|}, \tag{86}$$

and m is the (complex) refractive index of the ocean water. To take the effects of shadowing by surface waves into account, we multiply the ocean reflection matrix by a bidirectional shadowing function $S(\mu,\mu_0)$ given by [*Tsang et al.*, 1985]

$$S(\mu,\mu_0) = \frac{1}{1+\Lambda(\mu)+\Lambda(\mu_0)}, \quad (87)$$

where

$$\Lambda(\mu) = \frac{1}{2}\left\{\left[\frac{2(1-\mu^2)}{\pi}\right]^{1/2}\frac{s}{\mu}\exp\left[-\frac{\mu^2}{2s^2(1-\mu^2)}\right] - \mathrm{erfc}\left[\frac{\mu}{s\sqrt{2(1-\mu^2)}}\right]\right\} \quad (88)$$

and erfc(x) is the complementary error function. The Fourier components of the ocean surface reflection matrix are obtained by numerical Gauss integration in the formulas [cf. equation (12)]

$$\boldsymbol{R}_0^m(\mu,\mu_0) = \frac{1}{2\pi}\int_0^{2\pi} d\varphi\, \boldsymbol{B}^m(\varphi)\,\boldsymbol{R}_0(\mu,\mu_0,\varphi), \quad (89)$$

where

$$\boldsymbol{B}^m(\varphi) = \mathrm{diag}[\cos m\varphi - \sin m\varphi;\ \cos m\varphi - \sin m\varphi;\ \cos m\varphi + \sin m\varphi;\ \cos m\varphi + \sin m\varphi]. \quad (90)$$

Acknowledgments. We are grateful to B. E. Carlson, J. Chowdhary, J. E. Hansen, A. A. Lacis, W. B. Rossow, and M. Sato for many useful discussions, to J. Chowdhary for participating in an intercomparison of numerical accuracy of two radiative transfer codes, and to N. T. Zakharova for help with graphics. We thank J. L. Haferman, P. Stammes, and an anonymous reviewer for careful and constructive reviews. This research was funded by the NASA Earth Observing System Project managed by Goddard Space Flight Center in providing for the Earth Observing Scanning Polarimeter instrument analysis and algorithm development.

References

Ahmad, Z., and R. S. Fraser, An iterative transfer code for ocean-atmosphere systems, *J. Atmos. Sci.*, *39*, 656-665, 1982.

Bohren, C. F., and D. R. Huffman, *Absorption and Scattering of Light by Small Particles*, John Wiley, New York, 1983.

Charlson, R. J., S. E. Schwartz, J. M. Hales, R. D. Cess, J. A. Coakley, J. E. Hansen, and D. J. Hoffman, Climate forcing by anthropogenic aerosols, *Science*, *255*, 423-430, 1992.

Cox, C., and W. Munk, Statistics of the sea surface derived from Sun glitter, *J. Mar. Res.*, *13*, 198-227, 1954.

d'Almeida, G. A., P. Koepke, and E. P. Shettle, *Atmospheric Aerosols: Global Climatology and Radiative Characteristics*, 559 pp., A. Deepak, Hampton, Va., 1991.

de Haan, J. F., P. B. Bosma, and J. W. Hovenier, The adding method for multiple scattering calculations of polarized light, *Astron. Astrophys.*, *183*, 371-391, 1987.

DelGenio, T., Accuracy requirements, in *Long-Term Monitoring of Global Climate Forcings and Feedbacks*, edited by J. Hansen, W. Rossow, and I. Fung, *NASA Conf. Publ.*, *3234*, pp. 13-19, 1993.

de Rooij, W. A., Reflection and transmission of polarized light by planetary atmospheres, Ph.D. thesis, Free Univ., Amsterdam, 1985.

de Rooij, W. A., and C. C. A. H. van der Stap, Expansion of Mie scattering matrices in generalized spherical functions, *Astron. Astrophys.*, *131*, 237-248, 1984.

Deschamps, P.-Y., F.-M. Bréon, M. Leroy, A. Podaire, A. Bricaud, J.-C. Buriez, and G. Séze, The POLDER mission: Instrument characteristics and scientific objectives, *IEEE Trans. Geosci. Remote Sens.*, *32*, 598-615, 1994.

Deuzé, J. L., M. Herman, and R. Santer, Fourier series expansion of the transfer equation in the atmosphere-ocean system, *J. Quant. Spectrosc. Radiat. Transfer*, *41*, 483-494, 1989.

Diner, D. J., C. J. Bruegge, J. V. Martonchik, G. W. Bothwell, E. D. Danielson, E. L. Floyd, V. G. Ford, L. E. Hovland, K. L. Jones, and M. L. White, A Multi-angle Imaging SpectroRadiometer for terrestrial remote sensing from the Earth Observing System, *Int. J. Imaging Syst. Technol.*, *3*, 92-107, 1991.

Diner, D. J., W. Abdou, T. Ackerman, J. Conel, H. Gordon, R. Kahn, J. Martonchik, S. Paradise, M. Wang, and R. West, MISR level 2 algorithm theoretical basis: Aerosol/surface product, part 1 (aerosol parameters), Rep. *JPL-D11400*, Rev. A, Jet Propul. Lab., Pasadena, Calif., 1994.

Gordon, H. R., and M. Wang, Retrieval of water-leaving radiance and aerosol optical thickness over the oceans with SeaWiFS: A preliminary algorithm, *Appl. Opt.*, *33*, 443-452, 1994.

Hansen, J. E., Multiple scattering of polarized light in planetary atmospheres, II, Sunlight reflected by terrestrial water clouds, *J. Atmos. Sci.*, *28*, 1400-1426, 1971.

Hansen, J. E., and J. W. Hovenier, Interpretation of the polarization of Venus, *J. Atmos. Sci.*, *31*, 1137-1160, 1974.

Hansen, J. E., and A. A. Lacis, Sun and dust versus greenhouse gases: An assessment of their relative roles in global climate change, *Nature*, *346*, 713-719, 1990.

Hansen, J. E., and L. D. Travis, Light scattering in planetary atmospheres, *Space Sci. Rev.*, *16*, 527-610, 1974.

Hansen, J., W. Rossow, B. Carlson, A. Lacis, L. Travis, A. DelGenio, I. Fung, B. Cairns, M. Mishchenko, and M. Sato, Low-cost long-term monitoring of global climate forcings and feedbacks, *Clim. Change*, *31*, 247-271, 1995.

Hooker, S. B., W. E. Esaias, G. C. Feldman, W. W. Gregg, and C. R. McClain, An overview of SeaWiFS and ocean color, *NASA Tech. Momo.*, *104566*, 1992.

Hovenier, J. W., and C. V. M. van der Mee, Fundamental relationships relevant to the transfer of polarized light in a scattering atmosphere, *Astron. Astrophys.*, *128*, 1-16, 1983.

Hsiung, J., Mean surface energy fluxes over the global ocean, *J. Geophys. Res.*, *91*, 10,585-10,606, 1986.

Karl, T. R. (Ed.), Long-term climate monitoring by the global climate observing system, *Clim. Change*, *31*, 131-652, 1995.

Kaufman, Y. J., Remote sensing of direct and indirect aerosol forcing, in *Aerosol Forcing of Climate*, edited by R. J. Charlson and J. Heintzenberg, pp. 297-334, John Wiley, New York, 1995.

Kawabata, K., D. L. Coffeen, J. E. Hansen, W. A. Lane, M. Sato, and L. D. Travis, Cloud and haze properties from Pioneer Venus polarimetry, *J. Geophys. Res.*, *85*, 8129-8140, 1980.

King, M. D., Y. J. Kaufman, W. P. Menzel, and D. Tanré, Remote sensing of cloud, aerosol, and water vapor properties from the Moderate Resolution Imaging Spectrometer (MODIS), *IEEE Trans. Geosci. Remote Sens.*, *30*, 2-27, 1992.

Koepke, P., Effective reflectance of oceanic whitecaps, *Appl. Opt.*, *23*, 1816-1824, 1984.

Lacis, A. A., and M. I. Mishchenko, Climate forcing, climate sensitivity, and climate response: A radiative modeling perspective on atmospheric aerosols, in *Aerosol Forcing of Climate*, edited by R. J. Charlson and J. Heintzenberg, pp. 11-42, John Wiley, New York, 1995.

Lacis, A., J. E. Hansen, and M. Sato, Climate forcing by stratospheric aerosols, *Geophys. Res. Lett.*, *19*, 1607-1610, 1992.

Mishchenko, M. I., The fast invariant imbedding method for polarized light: Computational aspects and numerical results for Rayleigh scattering, *J. Quant. Spectrosc. Radiat. Transfer*, *43*, 163-171, 1990.

Mishchenko, M. I., Reflection of light by plane-parallel slabs containing randomly-oriented, nonspherical particles, *J. Quant. Spectrosc. Radiat. Transfer*, *46*, 171-181, 1991.

Mishchenko, M. I., Light scattering by size-shape distributions of randomly oriented axially symmetric particles of a size comparable to a wavelength, *Appl. Opt.*, *32*, 4652-4666, 1993.

Mishchenko, M. I., and L. D. Travis, Light scattering by polydispersions of randomly oriented spheroids with sizes comparable to wavelengths of observation, *Appl. Opt.*, *33*, 7206-7225, 1994.

Mishchenko, M. I., L. D. Travis, and D. W. Mackowski, *T*-matrix computations of light scattering by nonspherical particles: A review, *J. Quant. Spectrosc. Radiat. Transfer*, *55*, 535-575, 1996.

Nakajima, T., and M. Tanaka, Effect of wind-generated waves on the transfer of solar radiation in the atmosphere-ocean system, *J. Quant. Spectrosc. Radiat. Transfer*, *29*, 521-537, 1983.

Penner, J. E., R. J. Charlson, J. M. Hales, N. S. Laulainen, R. Leifer, T. Novakov, J. Ogren, L. F. J. Radke, S. E. Schwartz, and L. D. Travis, Quantifying and minimizing uncertainty of climate forcing by anthropogenic aerosols, *Bull. Am. Meteorol. Soc.*, *75*, 375-400, 1994.

Rao, C. R. N., L. L. Stowe, and E. P. McClain, Remote sensing of aerosols over the ocean using AVHRR data: Theory, practice and applications, *Int. J. Remote Sens.*, *10*, 743-749, 1989.

Santer, R., M. Deschamps, L. V. Ksanfomaliti, and A. Dollfus, Photopolarimetry of Martian aerosols, II, Limb and terminator measurements, *Astron. Astrophys.*, *158*, 247-258, 1986.

Sato, M., K. Kawabata, and J. E. Hansen, A fast invariant imbedding method for multiple scattering calculations and an application to equivalent widths of CO_2 lines on Venus, *Astrophys. J.*, *216*, 947-962, 1977.

Sato, M., L. D. Travis, and K. Kawabata, Photopolarimetry analysis of the Venus atmosphere in polar regions, *Icarus*, *124*, 569-585, 1996.

Takashima T., Polarization effect on radiative transfer in planetary composite atmospheres with interactive interface, *Earth Moon Planets*, *33*, 59-97, 1985.

Tomasko, M. G., and L. R. Doose, Photometry and polarimetry of Saturn from Pioneer 11: Observations and constraints on the distribution and properties of cloud and aerosol particles, *Icarus*, *58*, 1-34, 1984.

Toon, O. B., Modeling the relationships between aerosol properties and the direct and indirect effects of aerosols on climate, in *Aerosol Forcing of Climate*, edited by R. J. Charlson and J. Heintzenberg, pp. 197-214, John Wiley, New York, 1995.

Travis, L. D., Remote sensing of aerosols with the Earth Observing Scanning Polarimeter, in *Polarization and Remote Sensing*, edited by W. G. Egan, *Proc. SPIE, Int. Soc. Opt. Eng.*, *1747*, 154-164, 1992.

Travis, L. D., Earth Observing Scanning Polarimeter, in *Long-Term Monitoring of Global Climate Forcings and Feedbacks*, edited by J. Hansen, W. Rossow, and I. Fung, *NASA Conf. Publ.*, *3234*, pp. 40-46, 1993.

Tsang, L., J. A. Kong, and R. T. Shin, *Theory of Microwave Remote Sensing*, 613 pp., John Wiley, New York, 1985.

Ulaby, F. T., R. K. Moore, and A. K. Fung, *Microwave Remote Sensing*, II, pp. 922-1033, Addison-Wesley, Reading, Mass., 1982.

van de Hulst, H. C., *Light Scattering by Small Particles*, 470 pp., John Wiley, New York, 1957.

van de Hulst, H. C., *Multiple Light Scattering*, 739 pp., Academic, Dan Diego, Calif., 1980.

Wang, M., and H. R. Gordon, Estimating aerosol optical properties over the oceans with the multiangle imaging spectroradiometer: Some preliminary results, *Appl. Opt.*, *33*, 4042-4057, 1994.

West, A. R., and P. H. Smith, Evidence for aggregate particles in the atmospheres of Titan and Jupiter, *Icarus*, *90*, 330-333, 1991.

Wiscombe, W. J., On initialization, error and flux conservation in the doubling method, *J. Quant. Spectrosc. Radiat. Transfer*, *16*, 637-658, 1976.

M. I. Mishchenko and L. D. Travis, NASA Goddard Institute for Space Studies, 2880 Broadway, New York, NY 10025. (e-mail: crmim@giss.nasa.gov; pdldt@giss.nasa.gov)

(Received February 14, 1996: revised May 16, 1996; accepted June 25, 1996.)

CORRIGENDA

For your convenience, we are attaching correct versions of Figures 12 and 14a in which arrows show small details which have disappeared upon reproduction.

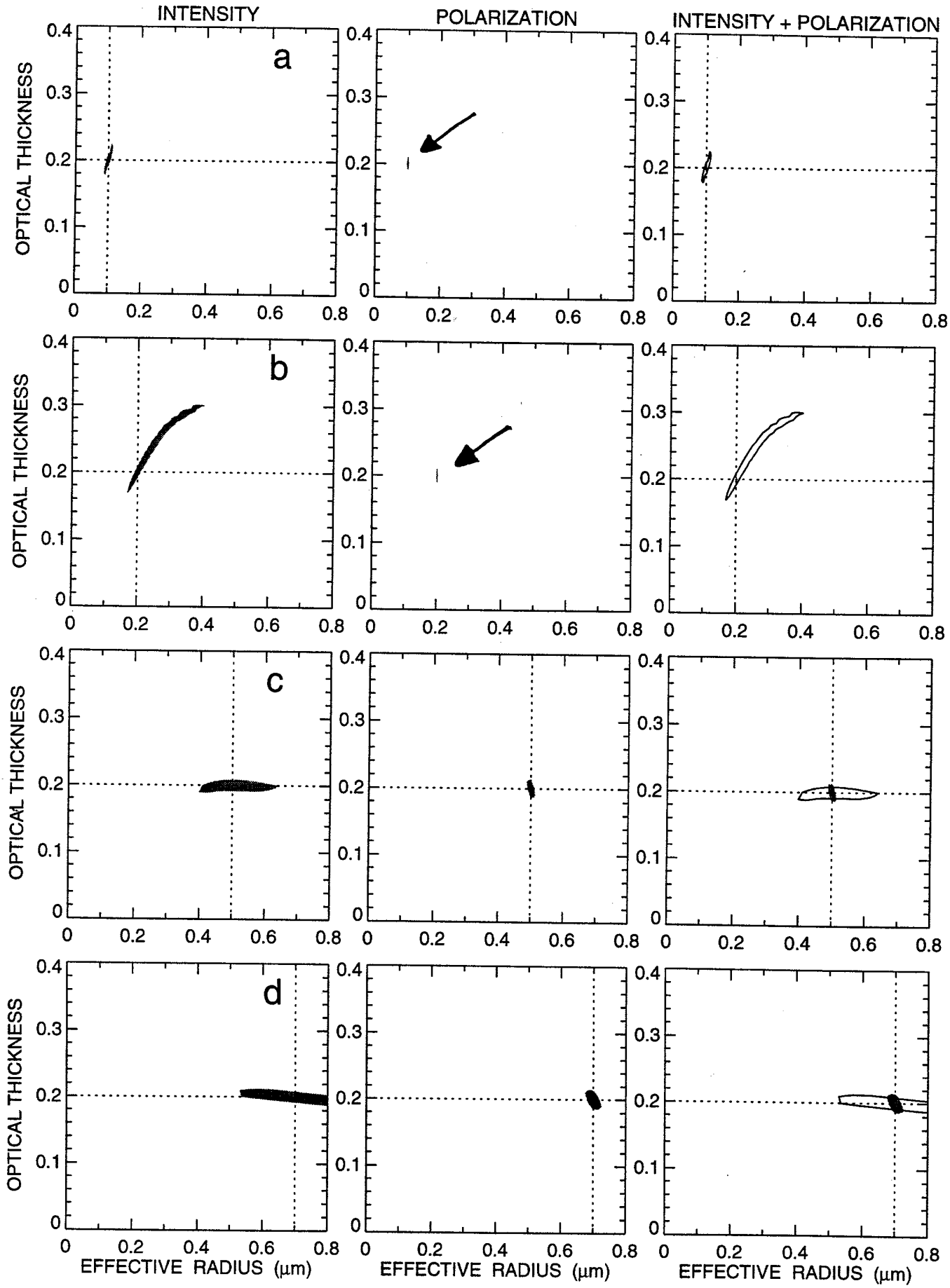
INTENSITY
POLARIZATION
INTENSITY + POLARIZATION
a
b
c
d
OPTICAL THICKNESS
EFFECTIVE RADIUS (μm)
0
0.1
0.2
0.3
0.4
0.6
0.8

Figure 12

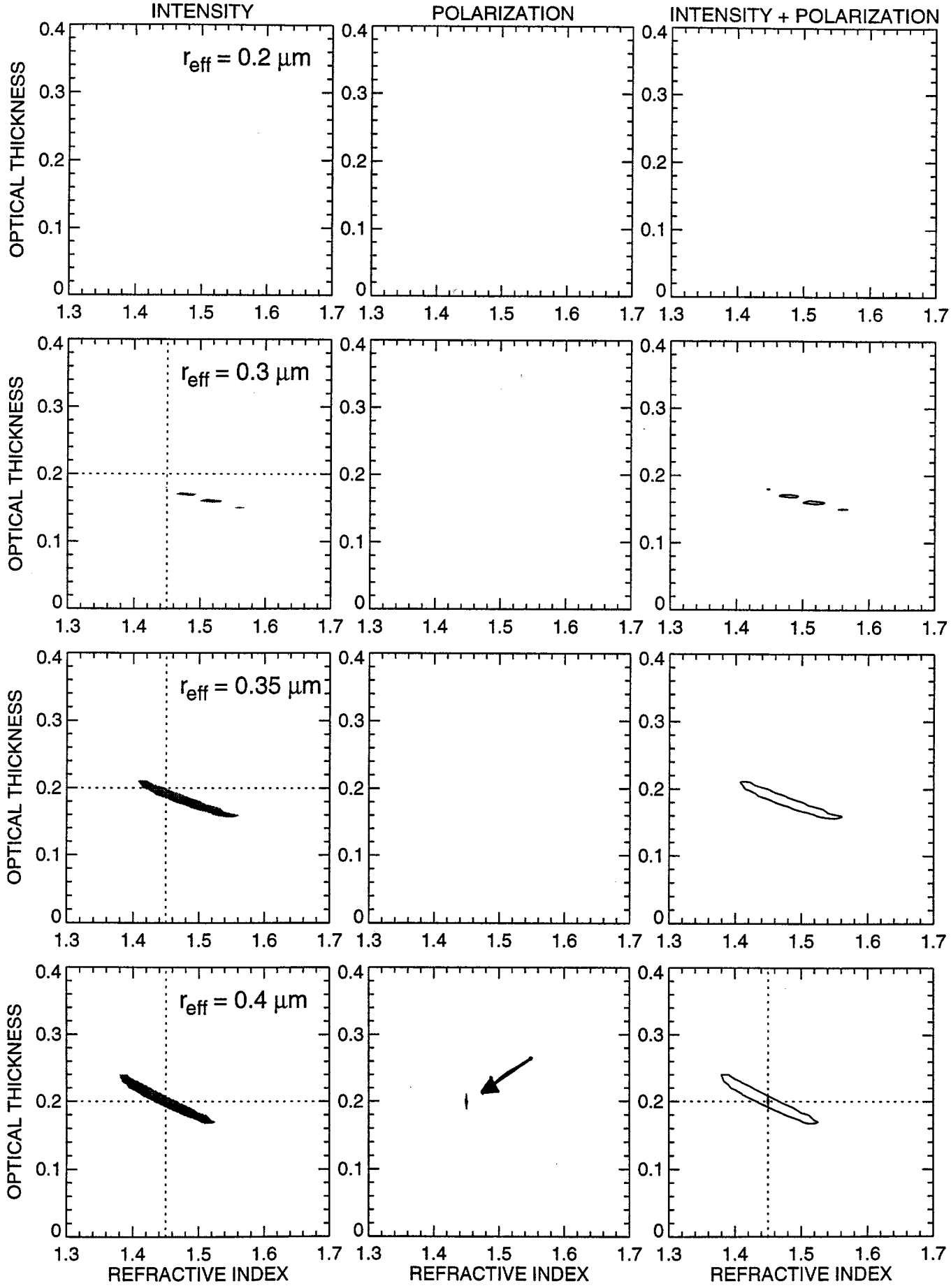
INTENSITY
POLARIZATION
INTENSITY + POLARIZATION
r_{eff} = 0.2 μm
r_{eff} = 0.3 μm
r_{eff} = 0.35 μm
r_{eff} = 0.4 μm
OPTICAL THICKNESS
REFRACTIVE INDEX
0.4
0.3
0.2
0.1
0
1.3
1.4
1.5
1.6
1.7

Figure 14a